School of Chemistry

Fabrication and Evaluation of Transmissive Diamond Dynodes

Simran Bath

This thesis is submitted in partial fulfilment of the requirements for the Honours Degree of MSci at the University of Bristol

Supervisor: Professor Neil Fox
Second Assessor: Professor Paul May
Physical and Theoretical Chemistry

Statement of factors which limited project progress

During the duration of this project there were a few disturbances, spanning approximately three weeks, that resulted in decreased time in the lab. This included repairs to air conditioning and extraction fans which hindered the use of equipment and prevented the use of gases, and therefore growths and terminations.

This primarily limited the amount of time spent on characterising the gain of the dynodes as the samples had to wait to be cleaned (requiring hydrogen plasma treatment) before surface termination. Therefore, initial plans to refine the experimental method were affected by this reduction in time. It also prevented further growths which reduced the number and variety of samples that could be produced, therefore ideas for samples with larger membranes or different patterning were not able to be fulfilled.

Abstract

Diamond has a plethora of properties which make it desirable for a vast range of applications, particularly within the electronics industry for its advantages in electron multiplication. This makes it ideal for use as a transmissive dynode to improve microchannel plate photomultiplier tubes by increasing gains and response times as well as preventing the degradation of the photocathode.

Two transmissive diamond dynodes, one polycrystalline and one single crystal, were fabricated and both involved a boron-doped diamond growth. They possessed membranes with a maximum thickness of 30 μm, achieved by laser micromachining, avoiding fractures by using a stepped membrane and careful control of laser power. The laser was also utilised to provide smoother surfaces which were able to be analysed with scanning electron microscopy.

Furthermore, functionalisation of the surfaces of the dynode involved a termination of lithium-oxygen (Li-O) on the output surface, carried out in Bristol's NanoESCA facility to achieve an NEA surface. This was able to be confirmed via X-ray photoelectron spectroscopy, which exhibited the presence of a Li_2O surface.

Upon analysis of the gain of the dynode, major charging up effects were seen from the large current emitted by the Kimble Physics electron flood gun therefore, an alternative method to characterise the dynode gain was developed. This involved a 255 nm UV LED that was used to irradiate a quartz disc with a 15 nm layer of gold deposited on the output surface. This intended to better simulate the current output of a photocathode and mitigate charging up effects that are commonly seen in dynode analysis. Although the analysis showed an improvement in charging up effects, this could be improved further by alterations to the experimental setup, particularly the grounding of the dynode.

The results showed that the SCD dynode performed better than the PCD with maximum gains of 4 - 5 compared to 3 - 4 for the PCD dynode. Even though some charging up was experienced, minimum gains still exhibited electron multiplication ($\delta > 1$). However, improvements to the gain would likely be seen by the use of an independent bias across the entire dynode as well as employing higher accelerating voltages.

Acknowledgements

I would like to express a great deal of gratitude to Professor Neil Fox for his constant support throughout the project and to the diamond lab. His availability and check-ins during the weekly meetings were extremely helpful throughout the entirety of this project. As well as this, I would like to thank Professor Paul May for his guidance and ideas and of course, for arranging the BUDGie meals which were a very special addition to the year.

Thank you to Dr. Liam Cullingford for all his help throughout the project, especially for the very fiddly setups that we managed to master. As well as this I would like to thank Catherine Monk for all of her support in the lab and for her expertise with the laser process. Also, to Dr. Ramiz Zulkharnay for his breadth of knowledge and help in the lab, answering all of my many questions. Finally, Dr. James Smith for all his expert knowledge and help throughout the project.

I would also like to show appreciation to Dr. Jude Laverock for allowing use of the NanoESCA facility and for carrying out the termination and XPS of my samples.

I would like to thank all my fellow BUDGies in the diamond lab. I was lucky to face the many surprises the lab had to offer with such a lovely group of people, and I wish them all the best for the future.

Finally, to my family for all their support throughout my time at university and to the best flatmates for lifting me up when I needed it.

Table of Contents

List of Figures

List of Tables

List of Abbreviations

HTHP	High Temperature High Pressure
CVD	Chemical Vapour Deposition
HFCVD	Hot Filament Chemical Vapour Deposition
MWCVD	Microwave-plasma Chemical Vapour Deposition
NEA	Negative Electron Affinity
PEA	Positive Electron Affinity
CB	Conduction Band
VB	Valence Band
DFT	Density Functional Theory
SEY	Secondary Electron Yield
SCD	Single Crystal Diamond
PCD	Polycrystalline Diamond
BDD	Boron-Doped Diamond
MCP	Microchannel Plate
PMT	Photomultiplier Tube
QE	Quantum Efficiency
CE	Collection Efficiency
ALD	Atomic Layer Deposition
TTS	Time Transit Speed
ML	Monolayer
UHV	Ultra-High Vacuum
SEM	Scanning Electron Microscopy
XPS	X-ray Photoelectron Spectroscopy
ICP-RIE	Inductively Coupled Plasma Reactive Ion Etching
IBE	Ion Beam Etching
BE	Binding Energy

1 Introduction

1.1 Diamond as a Material

1.1.1 Properties of Diamond

Diamonds are known for their use as gemstones in jewellery, adorning the necks and fingers of people around the world; however, they have many additional uses. One of the most common applications of diamond is for cutting and drilling because it is the hardest known material.[1] This is due to its giant covalent structure where carbon atoms form a rigid tetrahedral network with a face-centred cubic (FCC) structure and a lattice constant α = 3.57 Å, shown in Figure 1.[2] Each carbon atom is covalently bonded to 4 others from its 2s and three 2p orbitals, resulting in sp^3 hybridisation.[3]

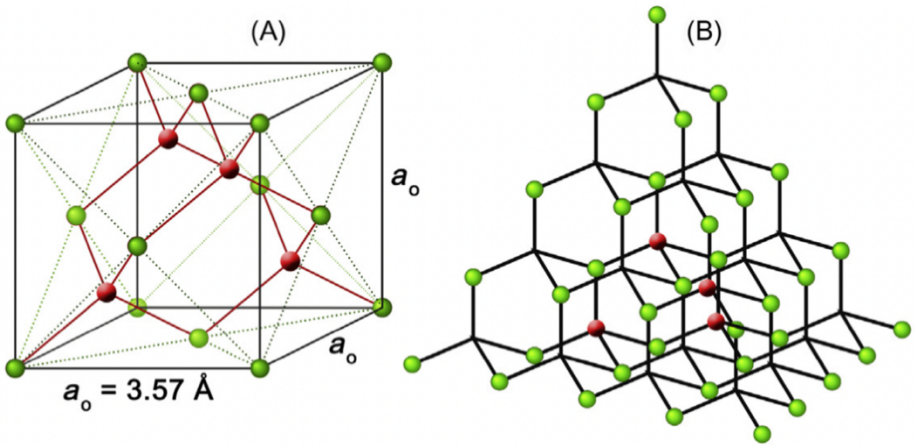

Figure 1: (A) Shows the face-centred cubic (FCC) structure of diamond. (B) Shows the giant tetrahedral network of diamonds covalent structure. Figure is taken from reference [2].

Additionally, diamond has a plethora of properties which exceed those of other materials, for example it has the highest thermal conductivity at room temperature, making it a great heat sink with applications in cooling electrical equipment.[4] As well as this, as it is transparent over a wide range of wavelengths, ranging from ultraviolet to the infrared, this makes it a great optical material to form components of laser and spectroscopy equipment.[5] Furthermore, it is also biologically inert and highly resistant to chemical corrosion which is beneficial for all uses of diamond as it can remain stable and unaltered in any harsh chemical environments it may be exposed to.[6] Due to its wide range of outstanding properties, diamond has applications spanning many industries from electronics to construction which highlights the need to continue to research this material.

In nature, diamonds are formed within the Earth's mantle, under intense heat and pressure from temperatures of 900 - 1,400 °C and pressures of 50 - 60 kbar.[7] However, in the 1950s these conditions were replicated under laboratory conditions forming the high-pressure high-temperature (HPHT) method.[8] This allows for the formation of diamonds without the ethical concerns with naturally formed diamond, as well as coming at a cheaper price. However, the diamonds formed from this method can possess flaws and impurities and they are also made in the form of single crystals that range from the nanometer to millimeter scale in size, which does not allow for its aforementioned properties to be truly utilised.[9]

1.1.2 The Theory of Diamond Growth

Rather than creating crystals of diamond, chemical vapour deposition (CVD) deposits a diamond coating onto a substrate as a thin film. This is a much more useful way to exploit the properties of diamond in real-life applications, for example as thermal management in electronic equipment.

First came the hot filament CVD (HFCVD) reactor, in 1982, which involves placing a suitable substrate in a vacuum chamber and exposing it to high temperatures (around 800 - 1000 °C). A refractory metal, like tungsten, is used as the hot filament while a controlled gas flow is introduced across the substrate.[8] This method is able to create diamond films however, the filament material often contaminates the diamond film while the filament itself is sensitive to oxidising or corrosive gases. Therefore, the choice of reactant gases are limited, restricting the types and applications of diamond films made.[9] This means these films are not as suitable for electronic purposes where purer diamond is required.

Microwave plasma-assisted CVD (MWCVD) was used for the first time a year later, in 1983. It employs similar conditions to HFCVD reactors, but instead microwave radiation is transmitted into the chamber by a dielectric window to create a localised gas plasma discharge.[9] This plasma creates many active species which leads to the deposition of a diamond film onto a substrate which could either be diamond, a carbide-forming metal or semiconductor (such as a silicon wafer) depending on the

desired application.[8] This results in higher growth rates and much purer diamond, as there is no filament to contaminate the diamond, and as well as this, a broader variety of gases can be used meaning this this is the top choice for CVD growth.[10]

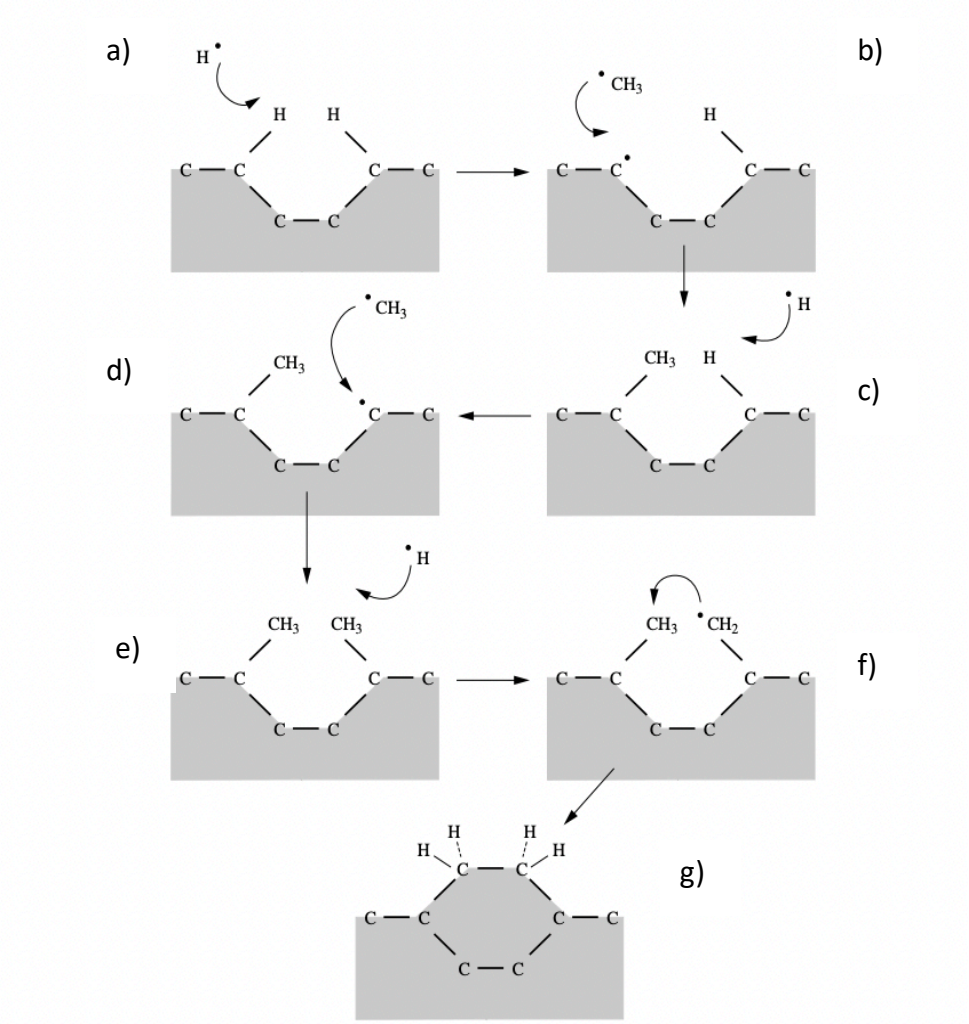

Figure 2: The stepwise growth of CVD diamond. Carbons are slowly added to the lattice, forming a diamond film. Figure is taken from reference [9].

The chemistry of CVD growth involves the reaction of carbon in the gas phase, usually in the form of methane (CH_4) diluted in hydrogen (H_2), which reacts with the chosen substrate. The process is outlined in Figure 2, first a H• radical reacts with a surface H atom to form molecular H_2 (a) which leaves a reactive site where a CH_3• radical could collide and react, adding a carbon to the lattice (b). However, the likelihood of an impinging CH_3• radical bonding to surface diamond carbon atoms is low due to the presence of hydrogen which can terminate surface carbons, or even displace them. Eventually this process is repeated at a neighbouring site (c-d) and then another H•

radical can remove a H atom from a CH_3 group, forming a CH_2• radical (e). This can then react with a neighbouring CH_3 group and eventually add a new layer of diamond to the lattice (f-g).[9] The process of laying down a surface carbon layer is very slow (*ca.* 5-10 μm h^{-1}) but the constant bombardment of the surface eventually leads to stepwise growth, forming a diamond film.

1.2 Functionalisation of Diamond Films

1.2.1 Negative Electron Affinity

For an electron to be emitted from a surface it requires enough energy to overcome the potential barrier at the interface between the surface and external environment, which is known as the work function.[11, 12]

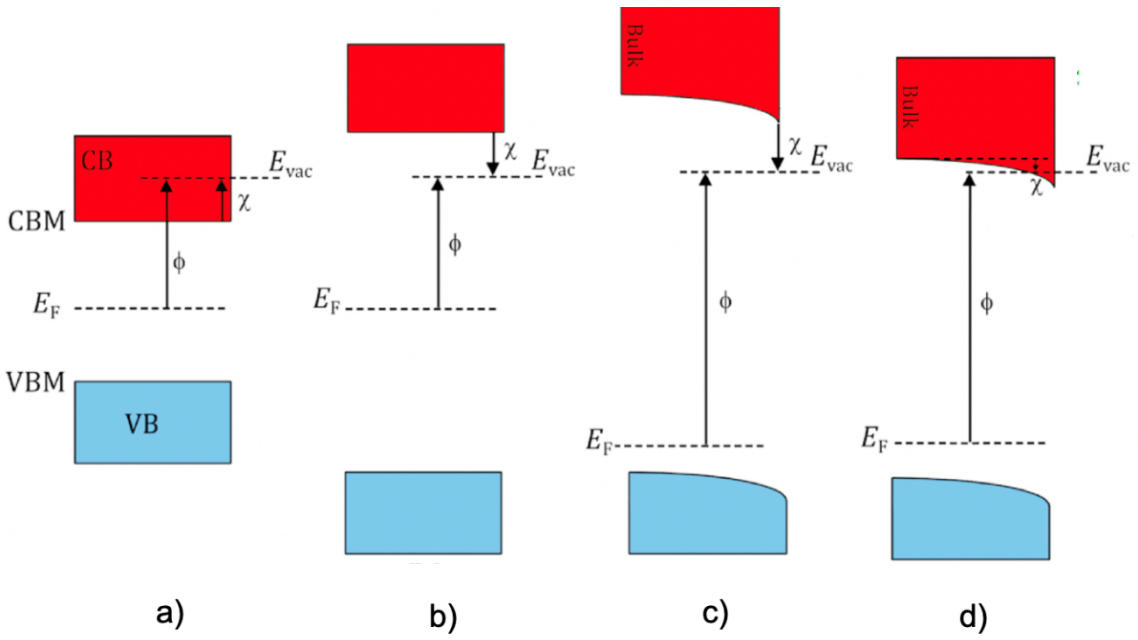

Figure 3: A comparison of positive electron affinity (PEA), true negative electron affinity (NEA) and effective NEA surfaces. (a) Shows a PEA surface, (b) shows a true NEA surface, (c) shows the downward band-bending as a result of p-type doping, still resulting in a true NEA surface and (d) shows an effective NEA surface as a result of p-type doping. Figure is taken from reference [12].

For typical semiconductors, the conduction band (CB) is usually empty, and the valence band (VB) is partially or fully occupied. They are usually separated by an

energy gap of 1 - 4 eV so UV photons or temperatures over 1000 °C are needed to be able to excite electrons to the CB or directly to the vacuum.[12] However, for certain materials such as diamond, the CB can lie higher in energy than the vacuum level and this is known as true negative electron affinity (NEA) as there is no barrier for the electrons in the CB to leave the surface, this is shown in Figure 3.[13] Therefore, the electrons in the VB only need to be excited into the CB for emission to occur therefore, less photons or thermal energy are needed which is very beneficial for applications where electron emission is required. Figure 3 also shows an effective NEA which can occur as a result of downward band-bending due to p-type doping. This can still maintain a true NEA surface, or the CB minimum may be pushed below the vacuum level. As the energy barrier is so small it is an effective NEA surface, but the presence of a barrier results in lower emission.[12]

1.2.2 Surface Termination

Diamond is able to possess an NEA, but this depends on the surface termination applied to the CVD film, an NEA surface only occurs when terminated with an electropositive chemical species, as shown in Figure 4.[13] Most commonly, CVD diamond is left with the hydrogen termination because it is already abundant in the mixture of gas that is used during MWCVD growth and so can suitably terminate the 'dangling' bonds from the surface carbon atoms. As well as this, H_2 gas is a necessary part of the gas mixture used as it will etch sp^2 carbon faster than sp^3 carbon and remove any graphitic sections from the surface of the CVD diamond. The presence of hydrogen also will break up long hydrocarbon chains, preventing the build-up of large structures and ensuring stepwise growth and co-ordination of the diamond carbon atom layers.[9]

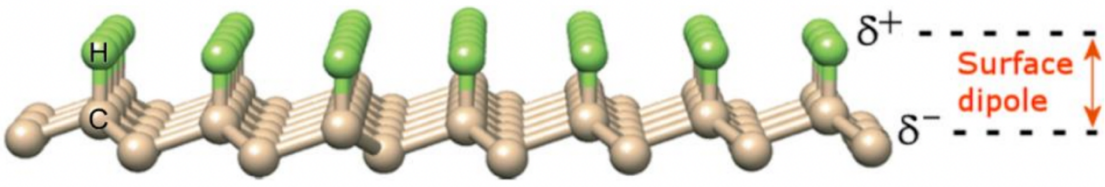

Figure 4: The dipoles that occur from surface termination with electropositive atoms. Figure is taken from reference [12].

The hydrogen terminated surface of diamond provides an NEA measured to be -1.3 eV on a C(100) surface and -1.27 eV on a C(111) surface.[14, 15] However, this surface termination readily degrades in air as the presence of water (H_2O) displaces the hydrogen with hydroxyl (OH) groups over time. Additionally, for electronic applications involving high currents, the movement of electrons through hydrogen terminated diamond can cause the H atoms to desorb, highlighting the need to investigate the use of other surface terminations.[9]

Therefore, there has been research into alternatives to hydrogen to provide an NEA surface with longer lifetimes. The use of alkali metals to terminate diamond was found to decrease the work function and give larger NEAs but it was when these metals were coated on oxygen terminated diamond that these effects were heightened while the stability showed great improvement.[13, 16] This is due to the high electropositivity of these metals which creates surface dipoles when bonded to the oxygen atoms which are then, in turn, bonded to the carbons on the surface of the diamond. Additionally, the improvement in stability can be attributed to the added strength from the M-O bonds over the M-C bonds.[11]

The use of lithium on an oxygenated surface is thought to make an effective surface termination, having one of the highest predicted NEAs, calculated through density functional theory (DFT) calculations.[16, 17] This can be seen in Table 1, in comparison to other commonly used surface terminations of diamond, Li-O has the highest theoretical NEA value and is on the higher end of reported values. This is because there is a strong binding affinity to the surface and as lithium is quite small, similar to the size of a carbon atom, a monolayer can easily be formed without issues that come from bigger atoms, such a caesium (Cs).[13] This is coupled with its large difference in electronegativity, to provide the ideal proposed NEA surface. A further aspect of the Li-O dipole formed on the diamond carbon surface is that unlike hydrogen, the dipole formed is bond-centred rather than atom-centred. This means that while the positive charge is localised on the Li-O bond, the negative charge appears on the O-C bond and the benefit of this is that the surface carbons more strongly feel the influence of the dipole.[18]

Table 1: A selection of commonly used surface terminations. This shows the theoretical NEA values (found from DFT calculations), some the highest reported NEA values and the thermal stabilities for each termination. All results were carried out using C(100) SCD for the purpose of a fair comparison.

Surface termination	Theoretical NEA value / eV	Reported NEA value / eV	Reported thermal stability / °C
Li-O	-3.9[16]	-2.1[19]	0-800[19]
Sc-O	-3.7[20]	-1.0[21]	0-700[21]
Mg-O	-3.2[18]	-2.0[22]	0-700[22]

This makes Li-O a great option for surface termination and the benefits that arise from a high NEA are very useful for many applications, especially those that require a high secondary electron yield (SEY).

1.2.3 Secondary Electron Yield

When materials that possess a high SEY are hit by primary electrons at high energies, multiple secondary electrons will be released.[5, 23] The movement of electrons through the material involves three stages; first the emitted electrons are excited to the bulk of the material, then they are transported to the solid surface and finally they leave the material to the vacuum.[24] With each collision, electrons will lose energy until they thermalise at the bottom of the CB which is why many materials, such as metals, do not exhibit a high SEY. However, diamond experiences efficient electron transport through the bulk of the material, where secondary electrons are able to be generated, to the surface.[5]

At the surface a potential barrier needs to be overcome however, diamond is an ideal material for this as its ability to possess an NEA eliminates this issue, providing a desirable SEY for electron multiplication purposes.

1.2.4 Surface Morphology

Depending on growth conditions, CVD diamond can come with many different surface morphologies. CVD diamond can be grown as single crystal diamond (SCD) or polycrystalline diamond (PCD). SCD has many different surfaces depending on crystal

orientation and the three most common orientations, shown in Figure 5, are octahedron C(111), cube C(100) and dodecahedron C(110).[25, 26] These have been shown to have different electrical properties as they will interact with electrons differently, resulting in different SEY and NEA values which highlights the need to consider the surface morphology.[27]

In terms of the surface termination of diamond, C(110) surfaces have been studied less as surface reconstruction is unfavourable and leads to fewer, less ordered dipoles therefore it is not the optimal orientation for an emission device.[28] High SEYs have been reported for C(100) and C(111) surfaces, however when involving a functionalised surface, the SEY achieved by the C(100) surfaces are higher.[27] This is due to different surface reconstructions as the C(100) surfaces have two dangling bonds per surface atom that will more readily bond to atoms, forming dimers.[29] In comparison, C(111) only has single dangling bonds that will bond to atoms less favourably, leading to a more tightly packed termination.[30] Therefore, surface termination is more effective with C(100) surfaces, and they are the better option when functionalising surfaces to achieve an NEA.

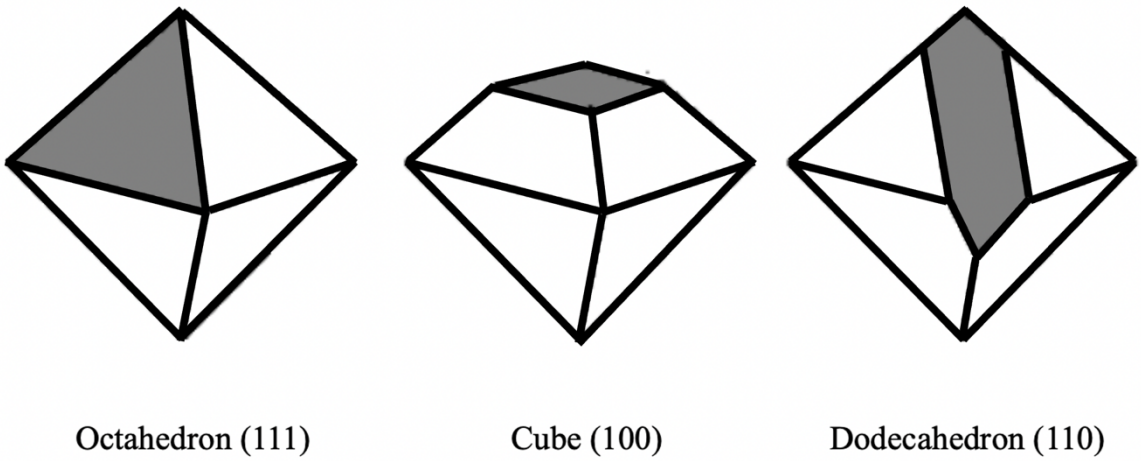

Figure 5: The common morphologies of diamond that are seen. Figure is adapted from reference [26].

While PCD contains an array of disordered crystal orientations, this is still relevant as grain size and boundaries can have an effect on the applications of PCD films. Growth conditions can be adjusted to better suit electronic purposes, as shown by the work of Vázquez-Cortés *et al.* where more crystals with (100) orientation can be introduced by increasing seeding density.[31]

1.2.5 Doping

For the many uses of CVD diamond, the semiconductor properties are one of its most beneficial, opening up the possibility of many electronic uses.[3] This means the diamond has a conductivity between an insulator and a conductor and relies on electrons being able to move from the VB to CB upon electrical stimulus.

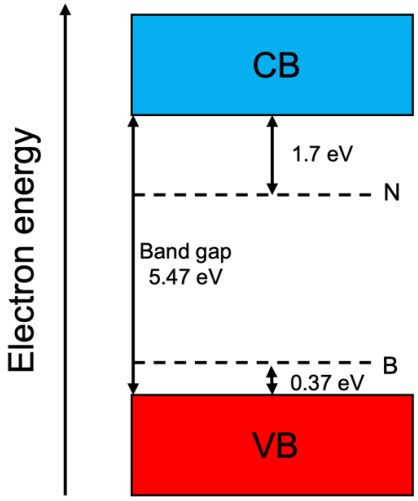

Figure 6: Bandgap diagrams of intrinsic and doped diamond. The lower accepting band is introduced from p-type doping and the higher donor band is introduced from n-type doping. Figure is adapted from reference [10].

To achieve this in diamond, it requires doping, which is where a chemical impurity is introduced to the lattice in order to increase conductivity. Materials can either experience n-type or p-type doping; the former involves introducing group 5 elements to create an excess of electrons, free to carry charge while p-type introduces group 3 elements to give a deficiency of electrons (known as holes) which electrons will move to fill.[32] This introduces a lower level accepting band, as shown in Figure 6, and the

movement of positively charged holes will increase the conductivity. To dope diamond, it is beneficial to use a dopant that is of a similar size to carbon, so that it can be easily integrated into the lattice, avoiding disruption to the structure. Therefore, if n-type doping is required, nitrogen will commonly be used and for p-type it is boron that is most commonly used, in the form of diborane (B_2H_6).[10]

As well as this, boron-doped diamond (BDD) can produce secondary electrons that allow for faster responses and reduced background noise due to their narrow energy distribution and low transverse energy, which makes it a great choice for electron multiplication applications.[33, 34]

1.3 The Applications of Transmissive Diamond Dynodes

1.3.1 Microchannel Plate Photomultiplier Tubes

Photocathodes are used to convert light into an electrical signal by emitting photoelectrons once photons are focused onto it. These can be collected and measured as electrical current, providing a quantitative measurement.[35] When the intensity of the light is low, there are not enough electrons emitted to produce a stable signal, therefore they need to be amplified.[5] This is usually obtained by devices such as microchannel plate photomultiplier tubes (MCP-PMTs); they can exhibit single-photon sensitivity accompanied with a very low level of noise and have many uses from night vision equipment to PET scanners.[33, 36]

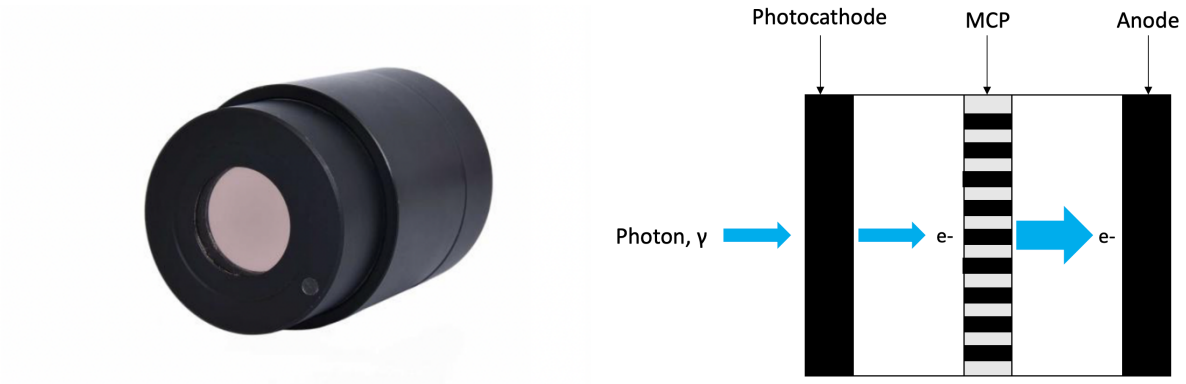

Figure 7: An MCP-PMT (left) and a simplified diagram showing its function (right). The pictured MCP-PMT is taken from reference [36] and the diagram was made using reference [41].

The structure of an MCP-PMT, as shown in Figure 7, involves a stimulated photocathode that emits electrons, and they work by applying high voltages to low energy electrons to then accelerate them to high velocities where they then reach an MCP.[37] The MCP consists of a substrate, typically made from borosilicate or lead glass, and contains many cylindrical channels with diameters of 4-25 μm.[38] They work to multiply the incident electrons by utilising the effects of a high SEY material and this resulting amplified current can then be detected.[39]

1.3.2 Limitations of MCP-PMTs

There are many applications for MCP-PMTs as photon sensors in particle physics experiments. They have uses in particle acceleration, fluorescence and phosphorescence experiments, where single photon counting is required.[40, 41] These experiments would benefit from better functioning amplifiers, with high gains and fast response times, providing improvements in applications from biological imaging to organic light emitting diodes (OLEDs).[42, 43] As well as this, uses involving detection of cosmic rays and Cherenkov radiation require higher quantum and collection efficiency.[44, 45] Quantum efficiency (QE) is a measure of how effectively a photocathode converts photons into electrons while collection efficiency (CE) refers to the fraction of photoelectrons collected by the anode, shown by equations 1 and 2.[46]

$$QE = \frac{Number\ of\ emitted\ photoelectrons}{Number\ of\ incident\ photons} \qquad \text{Eq. (1)}$$

$$CE = \frac{Number\ of\ detected\ photoelectrons}{Number\ of\ emitted\ photoelectrons} \qquad \text{Eq. (2)}$$

Overall, high energy physics experiments require photoelectron amplifiers that would benefit from high gains and fast response times. This will provide improvements in single photon counting experiments resulting in improved detection.[47]

Furthermore, a major drawback to MCP-PMTs is that their lifetimes can be affected by atoms of residual gases that may become ionised in the microchannels of the MCP.

These will instead accelerate towards the photocathode, because of the bias voltage, poisoning it over time.[48, 49]

Methods to resolve this have been investigated, as shown in Figure 8, for example a coating of aluminium oxide (Al_2O_3) by atomic layer deposition (ALD) on the microchannels of MCPs has been attempted to prevent any damaging contaminants desorbing from the pores of the MCP.[48] This was found to significantly improve lifetimes of MCP-PMTs however, there were some drawbacks including low current saturation levels, increased sensitivity in magnetic fields as well as increased gain recovery times.[40, 50] The use of a physical barrier has also been attempted in order to prevent the feedback of accelerated ions reaching the photocathode, for example the use of thin film of Al_2O_3 was investigated however, as may be expected, major decreases in transmission times and QE were also experienced.[48]

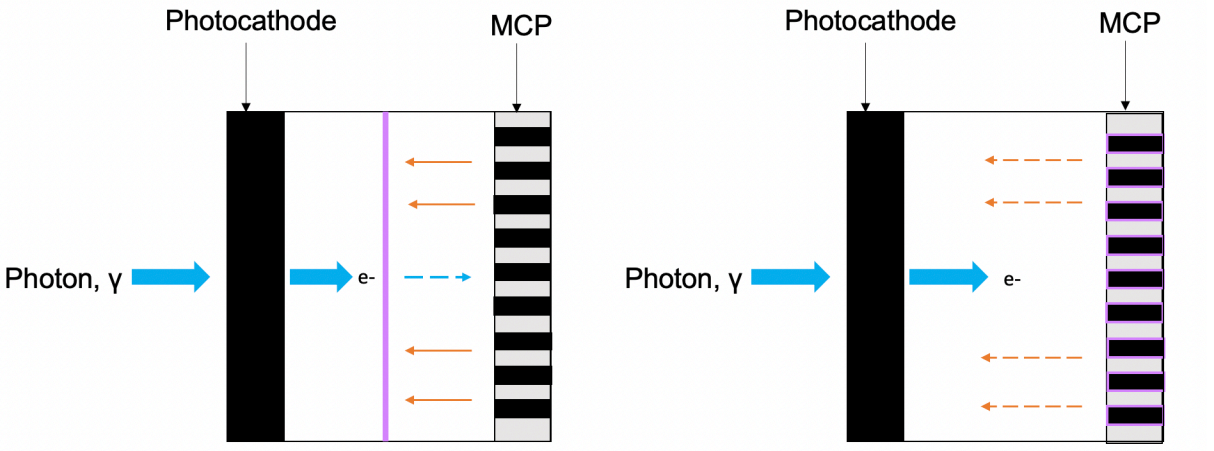

Figure 8: Shows methods employed to improve MCP-PMT performance. The left shows the insertion of a thin Al_2O_3 film (purple), preventing electrons reaching the photocathode but resulting in reduced QE. The right shows the coating of the channels of the MCP by ALD reducing backwards emission of electrons. Figure adapted from reference [51].

This therefore highlights the need for further improvements to the MCP-PMT structure in order to help improve photocathode lifetimes but also maintain a high efficiency so that they can be used for their desired purposes.

1.3.3 Dynodes

Dynodes are thin electrode membranes that are used for purposes of electron multiplication to amplify a small current into one that can be quantified and recorded.[35] There are two common types of dynodes, known as reflection and transmission dynodes, and they have different mechanisms of working, as shown in Figure 9. Reflective dynodes involve the emission of electrons from the same surface that was hit by the incident beam, and by angling multiple of these high SEY surfaces, significant electron multiplication is able to take place. Meanwhile transmission dynodes, as the name might suggest, emit electrons from the opposite surface that is struck and includes multiple stages for electrons to pass through, and in turn multiply.[23, 33]

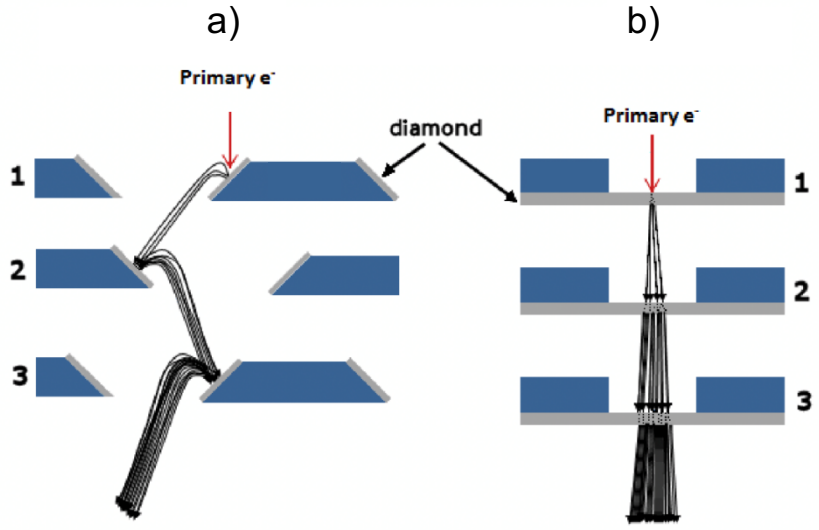

Figure 9: The two types of dynodes. (a) Shows the mechanism of reflective dynodes while (b) shows the mechanism of transmission dynodes. Figure is adapted from reference [23].

However, there are key benefits that have been identified with using transmission dynodes over reflective ones. Firstly, transmission dynodes are thought to prolong lifetimes of equipment as any high energy electrons, that may bombard and damage particle counters, will pass through the dynode and be slowed, instead releasing secondary electrons. Additionally, transmission dynodes have shown to have short total transit and dead times as well as uniform responses over large areas.[52]

Furthermore, transmission dynodes can prevent the feedback of charged particles to the photocathode, providing a physical barrier of protection. Therefore, the use of a transmission dynode could mitigate the lifetime related issues that are experienced by MCP-PMTs as it would physically protect the photocathode from the backward accelerating ions.

1.3.4 Diamond Dynodes

The use of diamond to fabricate a dynode provides the high SEY that is required, higher than many metals and insulators with reported gains of 80 (for SCD) and 10 (for PCD).[53, 54] The high SEY also allows for a better response time for detectors as this is determined by the time transit speed (TTS). This refers to the time taken for electrons to travel through all gain stages to the detector therefore, a higher SEY material means fewer stages, resulting in a lower TTS and improved response times.[37] This, in conjunction with its NEA surface which means the potential barrier is removed, makes for a very effective dynode which will require very little energy to free secondary electrons. Furthermore, the previously mentioned properties of diamond mean the dynode will be very stable and can withstand the effects of ion bombardment well.

This improved SEY combined with the NEA surface that is possessed by diamond, with the correct surface termination, will make for an effective transmission dynode and provide improvements in electron multiplication applications.

1.4 Project Aims

The aim of this thesis is to fabricate a PCD and SCD transmissive dynode. The general structure is shown in Figure 10, both will contain a BDD layer and the results of each can then be compared.

Transmission dynodes require especially thin membranes as the electron pulse has to pass through many stages and if this is too thick, then the efficiency will experience great reduction.[52, 55] Therefore, thin membranes will be achieved with laser micromachining, with particular emphasis to achieve smooth membranes to prevent electron scattering and improve dynode performance.

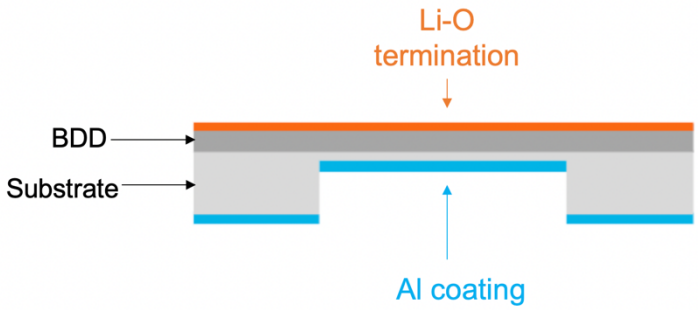

Figure 10: The intended structure of the transmissive dynode to be fabricated.

To achieve an NEA surface, the dynode will be terminated with Li-O due to its ability to provide large NEA values. The back of the dynode will be coated with a layer of aluminium in order to provide an electrical contact on the dynode, allowing for a bias voltage to be applied, while the physical metal layer should also prevent any secondary electron back emissions.

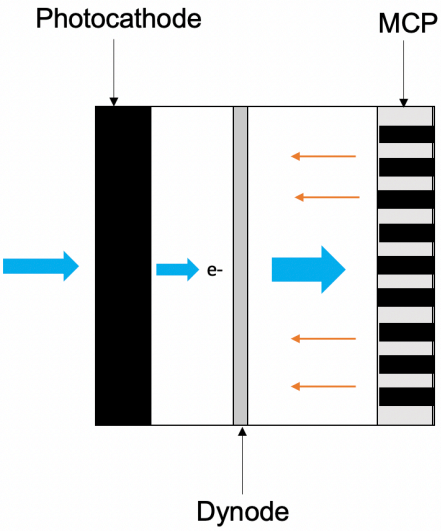

Figure 11: The insertion of the transmissive diamond dynode into the MCP-PMT setup. This would result in amplified current and protection of the photocathode.

As Figure 11 shows, dynodes are commonly used with photocathodes in an MCP-PMT setup. Therefore, an electron beam will be used to simulate these effects in order to evaluate the performance of the dynode. As well as this, scanning electron microscopy (SEM) and X-ray photoelectron spectroscopy (XPS) will be used to further characterise the surface of the dynode.

2 Experimental

2.1 Fabrication of Dynode

2.1.1 Diamond Growth

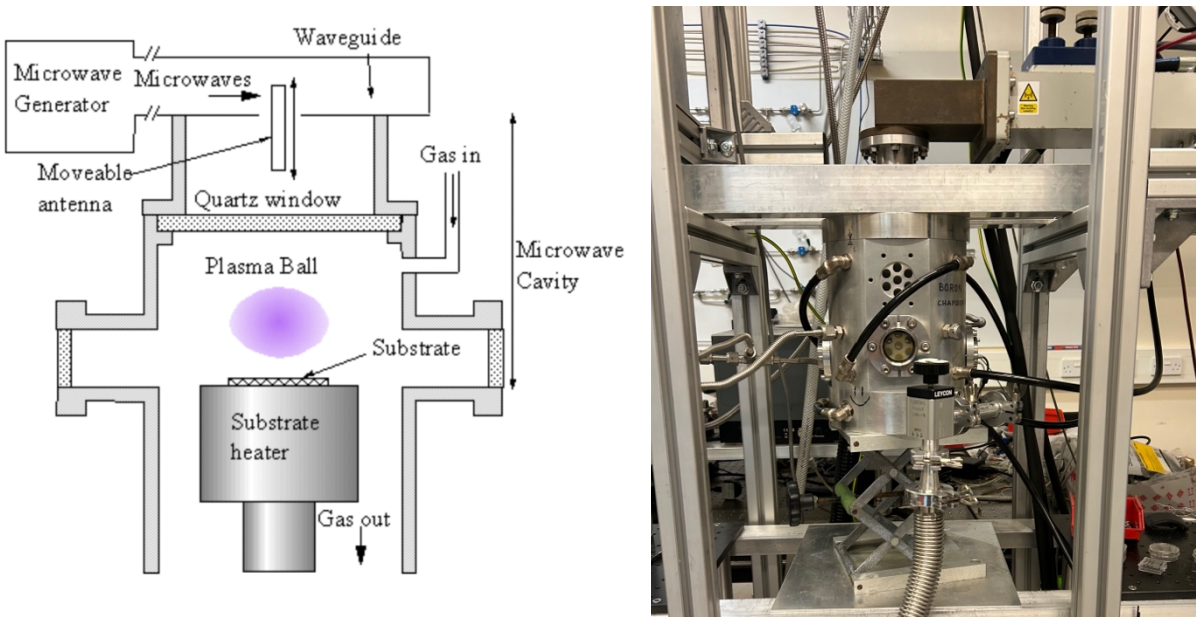

Figure 12: The ASTeX-type MWCVD reactor used for diamond growth. Figure shows a schematic (left) and the pictured setup (right). Schematic is taken from reference [56].

An ASTeX-type MWCVD reactor, Figure 12, was used to perform a 2 hour boron-doped diamond growth on a 10x10 mm polycrystalline diamond (PCD) Element Six tm180 substrate (Sample 1).[56] The conditions for the growth can be found in Table 2, the CH_4, H_2 and B_2H_6 (5%, H2 matrix) were research grade (> 99.99999 % purity). This was repeated on a second PCD substrate using the same conditions (Sample 2).

Table 2: Conditions used for boron-doped diamond growth on PCD substrates.

Parameter	Sample 1	Sample 2
Power / kW	1.2	1.2
Pressure / Torr	120	120
Temperature / °C	854 - 1023	831 - 969
Length / hour	2	2
H_2 flow rate / sccm	300	300
CH_4 flow rate / sccm	12.5	12.5
B_2H_6 flow rate / sccm	0.6	0.6

Additionally, a 6x6 mm Element Six single crystal diamond (SCD) C(100) sample (Sample 3) was provided in order to be analysed further and the conditions used for this growth can be found in Table 3.

Table 3: Conditions used for boron-doped diamond growth on SCD substrate. Note this was completed by a previous student.

Parameter	Sample 3
Power / kW	1.4
Pressure / Torr	140
Temperature / °C	870 - 950
Length / hour	2
H_2 flow rate / sccm	300
CH_4 flow rate / sccm	12.5
B_2H_6 flow rate / sccm	0.7

2.1.2 Laser Micromachining

In order to achieve a thin emission area, laser micromachining was employed. This involved the use of an Oxford Lasers Alpha 532-XYZ-AU micromachining system, shown in Figure 13. By pulsing a 532 nm laser at different powers, different amounts of diamond could be ablated. First the laser causes a graphitic change in the top surface of the diamond and then with further passes this is removed, etching away the diamond.[57]

Figure 13: The Oxford Lasers micromachining system used for the membrane process.

ALPHACAM computer-aided design (CAD) software was used to make the etching patterns. To also aid achieving the smoothest surface from the laser, the membrane is designed to be lasered in a cross hatched pattern; by minimising the beam width, this can be as thin as possible resulting in a very tight cross hatch network and overall smoother membrane.

An overview of powers and amount of diamond removed can be seen in Table 4, a process of slowly powering down the laser as the membrane gets thinner was utilised in order to prevent fracturing of the membrane. In the final few passes, the power was reduced between 10 - 5 % and the speed was increased to help etch away the peaks that were formed from the grooves left from the laser beam. This was also coupled with changing the Z focus; in early stages having a more focused beam was important to remove more diamond but towards the end the focus was shifted so the laser was further away which worked to provide more diffuse laser ablation and improve the smooth surfaces.

Table 4: Parameters used for laser micromachining of the diamond membranes.

Parameter	Value
Power / %	5 - 35
Pulse frequency / kHz	25
Beam width / mm	0.005 - 0.0075
Etch speed / mm s^{-1}	2

The PCD substrate used was a 10x10 mm substrate which is relatively large for dynode devices compared to previously made dynodes. Therefore, to provide more structural integrity, a stepwise membrane from 8x8 mm to 2x2 mm was employed, which can be seen in Figure 14. This allowed the membrane to be made much thinner, which is crucial for electron multiplication purposes. If the membrane was made 8x8 mm this would have taken a very long time to get it to appropriate thickness (due to the thin cross hatching) and it would have likely fractured before it was able to reach its thinnest using this method. A summary of the membrane process can be found in Table 5 which shows at what thickness the next step of the membrane was started, and this was found to provide good structural stability.

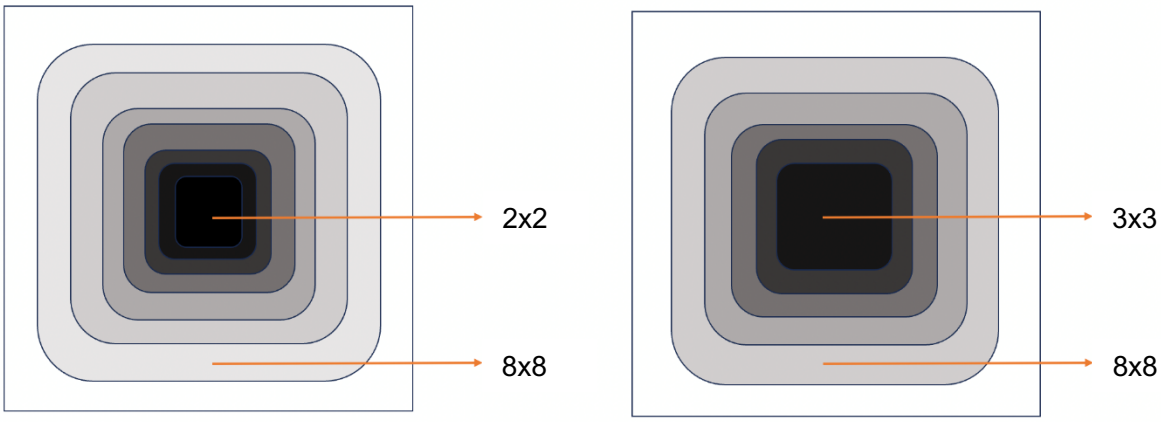

Figure 14: The design of stepwise membranes utilised for the PCD dynodes.

Table 5: The thickness of each step of the membrane. This was the thickness recorded before the next step down in the membrane process was started.

	Thickness remaining (before starting membrane) / μm	
Membrane size / mm	Sample 1	Sample 2
8x8 (starting thickness)	270	320
7x7	220	N/A
6x6	170	250
5x5	140	180
4x4	100	100
3x3	70	60
2x2	50	N/A

Due to the time restraint of this project, the second sample was also etched in a stepwise fashion, but this time the aim was to progress from an 8x8 mm membrane to 6x6 mm and finally 4x4 mm. This would make for a quicker process and a bigger recess that could be compared to the first sample. After the first sample experienced a fracture, this plan was adapted therefore the stepwise membrane misses out the 7x7 mm membrane, but this time the same thickness was achieved at a 3x3 mm recess as a compromise between the two original plans for the dynodes.

The SCD sample (Sample 3) that was provided already had a 3x3 mm etched recess, however this was 125 μm thick and so this was further etched to match the thickness of the PCD membranes. As this sample was much smaller than the others, a stepped membrane was not necessary but the same parameters in Table 4 were used.

Between each pass, the sample was sonicated in isopropanol (Fisher Scientific, > 99 % purity) for one minute in order to remove some of the graphitic build up from the laser process.

2.1.3 Hydrogen Plasma Etching

Once the membrane was complete, the samples were cleaned of all graphitic residue left from the laser process. This was done by placing the samples in a hydrogen plasma at a power of 0.9 kW and pressure of 90 Torr for 10 minutes followed by an

increase to 1.15 kW and 115 Torr for the last 5 minutes to ensure the graphite had been removed, as shown in Table 6.

Table 6: Conditions used for the hydrogen plasma clean of each of the samples.

Parameter	Sample
Power / kW	0.9 - 1.15
Pressure / Torr	90 - 115
Temperature / °C	700 - 790
Length / min	15
H_2 flow rate / sccm	300

The removal of graphite was monitored by an orange hue to the plasma, as shown in Figure 15, which was due to the graphite being removed. Once the graphitic surface was etched, the plasma appeared much more purple which is characteristic of a hydrogen plasma.

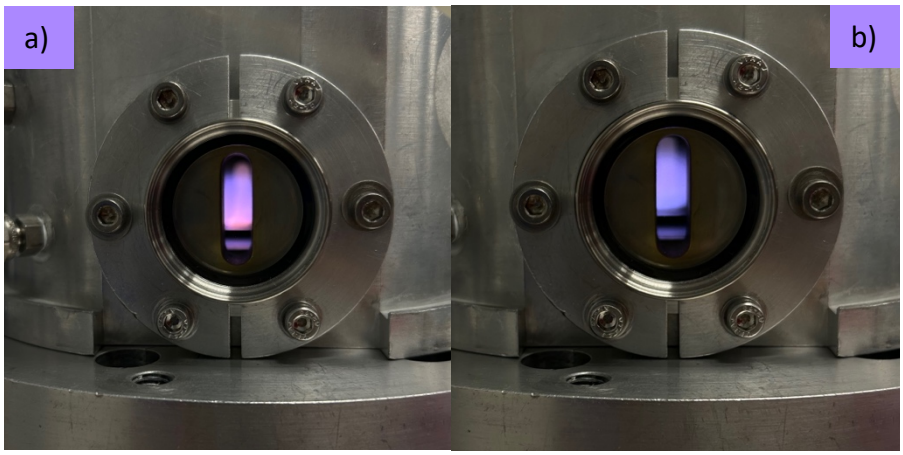

Figure 15: A comparison of the plasma during the hydrogen plasma etch. (a) Shows the plasma with an orange hue at the start of the etch due to the presence, and removal, of graphite. (b) Shows the purple hydrogen plasma at the end of the clean.

2.1.4 Aluminium Deposition

Aluminium (Al) was thermally evaporated using the Balzer's 510 coater to deposit 22.6 nm on the backside of the PCD dynode. The edges were masked using Kapton tape

leaving a 1 mm boarder around the outside to prevent charge flow paths forming. The Al serves as an electrical contact so the dynode can be biased during the testing process but also the layer of Al could prevent any back emission of electrons from the dynode.

This was only performed on the PCD dynode as the SCD dynode would be tested with the boron layer on the input surface, which can be seen in Figure 16, and this would act as the conducting contact.

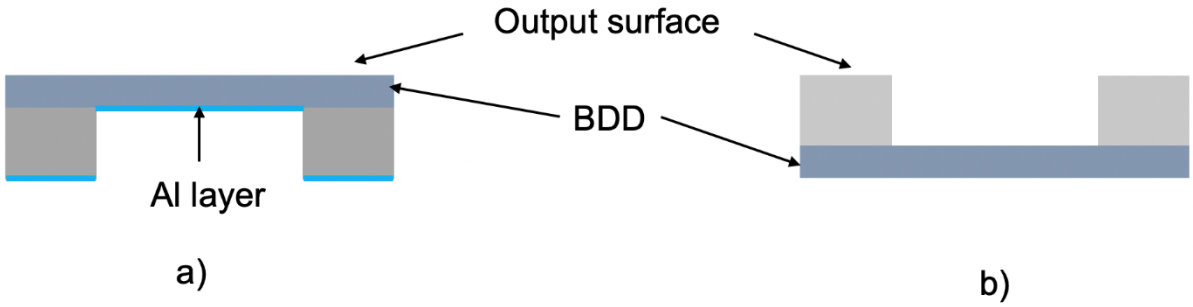

Figure 16: The differing structures of the PCD and SCD dynodes. (a) Shows the PCD dynode with an Al contact on the input surface and BDD on the output surface. (b) Shows the SCD dynode with BDD on the input surface.

2.1.5 Surface Termination

Following the deposition of Al on the back surface, the PCD sample was then loaded into the NanoESCA facility at the University of Bristol.

First, the sample was annealed at 900 °C under ultra-high vacuum (UHV) for the removal of any adsorbates or H termination on the surface. Next, it was exposed to molecular oxygen (Messer CANgas, 99.999% high-purity) for 5 minutes at room temp at a pressure of 1 x 10^{-2} mbar.

This was followed by a deposition of a 2/3 ML (monolayer) of Li by the exposure of the sample to thermally evaporated Li wire (Sigma-Aldrich/Merck, high-purity 99.9%) at 485 °C for 203 seconds. The pressure in the deposition chamber was 1 x 10^{-7} mbar during deposition. A surface activation anneal was then performed under UHV at 500 C for 30 minutes.

The O_2 exposure, Li deposition and final annealing steps were repeated twice more for a total of 3 depositions of this surface termination to achieve a more stable termination and lower negative electron affinity.

This process was also repeated for the SCD dynode but this time on the opposite surface to the PCD dynode, shown in Figure 17, so the laser-etched surface received the Li-O termination.

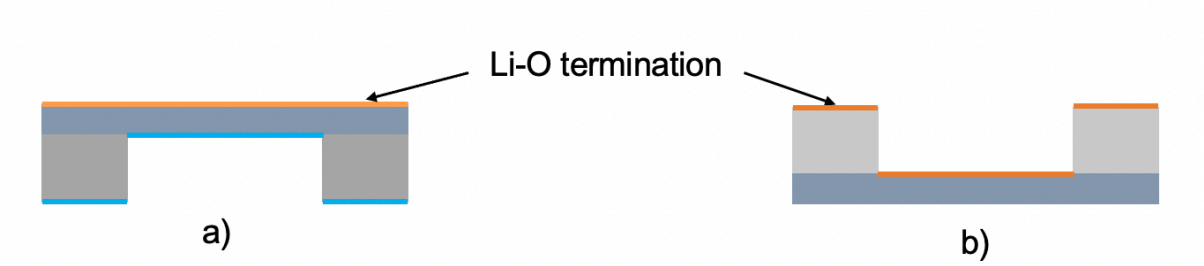

Figure 17: The dynodes after surface termination. The PCD dynode (a) terminated on the surface that was grown while the SCD dynode (b) was terminated on the laser-etched surface.

2.2 Characterisation Techniques

2.2.1 LEXT Laser Microscope

The Olympus LEXT OLS5100 laser scanning confocal microscope was very beneficial throughout the course of this project. As shown in Figure 18, it functions with a 405 nm laser that is able to scan the sample in the X, Y and Z directions, allowing a three-dimensional image of the sample to be made. By using a focused a laser with a beam diameter of 0.4 μm as the light source, better images can be made by reducing unnecessary scattered light, like with ordinary optical microscopes.[58, 59]

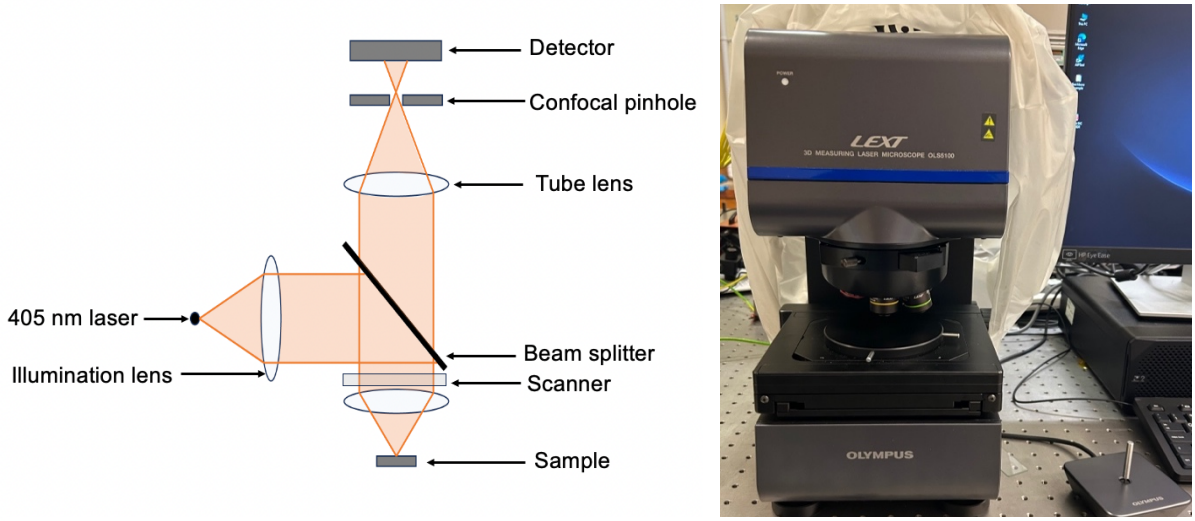

Figure 18: The LEXT laser microscope used for analysis. The left shows a simplified diagram showing the setup of a laser scanning confocal microscope, like the LEXT microscope which is pictured on the right. The schematic is adapted from references [58] and [59].

Due to this high-quality imaging, the LEXT was very useful in getting accurate height profiles of the sample (following a noise and tilt correction) during the membrane process as well as investigating surface features and providing three-dimensional imaging of the structures.

2.2.2 Scanning Electron Microscopy

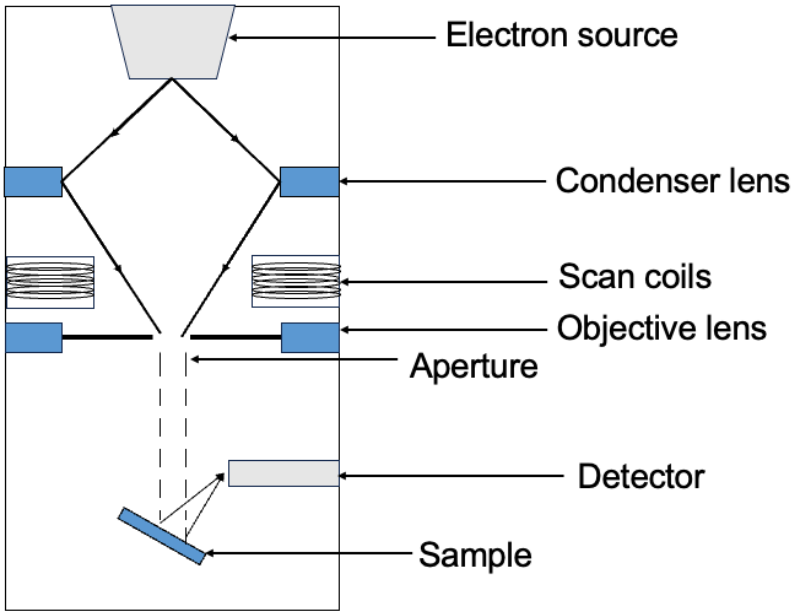

Figure 19: Simplified schematic of the SEM used for analysis. This figure was adapted from reference [60].

A JEOL IT300 scanning electron microscope was used to analyse the surface of the samples. It works by heating tungsten to emit electrons which are focused onto the sample and the reflected electrons are collected by the detector, forming an image, as can be seen in Figure 19.[60, 61]

SEM images were collected on the side that was etched by the laser with magnifications ranging from 16x - 100x at working distances of 10 - 27 mm.

This was carried out on Sample 1 but unfortunately it fractured when it was removed from the carbon tape. Therefore, SEM analysis was not repeated and only Sample 2 and Sample 3 experienced surface termination and analysis of their gains. In the future no physical strain should be used to remove the sample from the tape and instead it could be soaked in IPA and simply peeled off.

2.2.3 Raman Spectroscopy

The Renishaw Ramascope 2000 Raman system was used to analyse the composition of the samples. A simplified diagram of the system can be seen in Figure 20; the sample is hit by a laser with a wavelength of 514 nm which is then passed through filters to remove any Rayleigh scattering and then it reaches the detector.[62, 63]

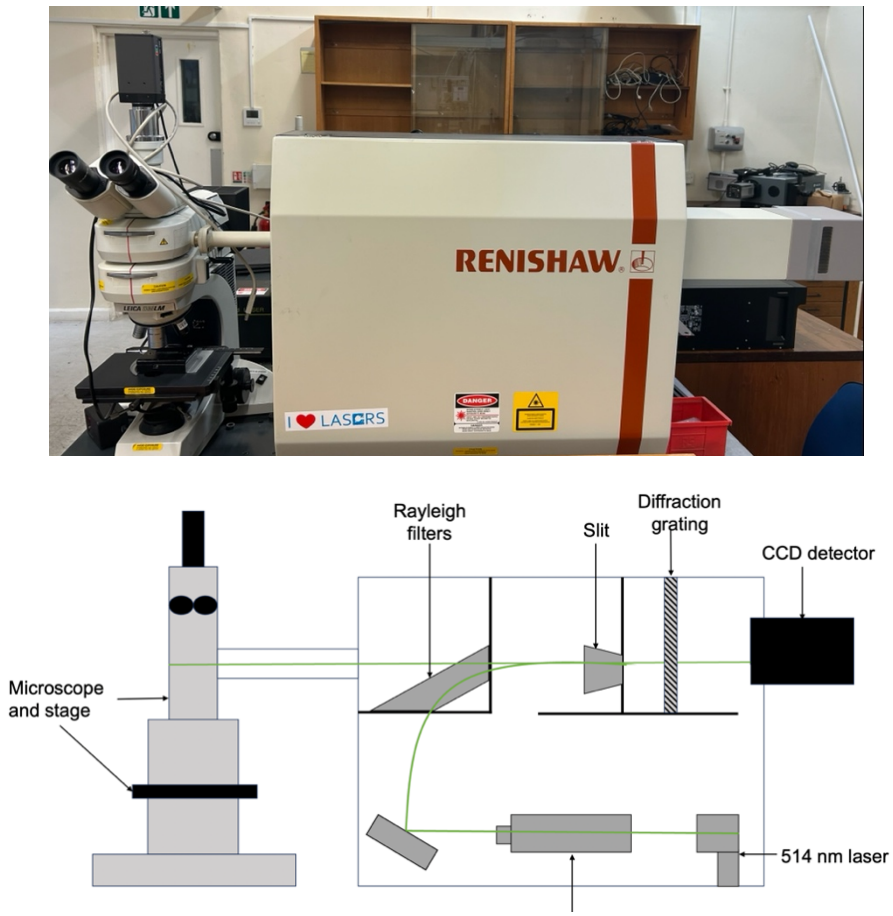

Figure 20: The Renishaw Raman spectrometer used for analysis. Figure shows the pictured setup (top) and a simplified schematic of the system (bottom). The schematic was adapted from reference [62].

Before a scan of the samples was acquired, it was first calibrated with a high purity SCD sample to ensure the diamond peak occurred at 1332 cm^{-1}.

Acquisitions were then taken by collecting 3 accumulations at 15 s exposure time and 10 % power. This was carried out directly after the lasering process and once the sample was cleaned in the hydrogen plasma to ensure the graphite was removed.

2.2.4 X-Ray Photoelectron Spectroscopy

During the surface termination process, X-Ray photoelectron spectroscopy (XPS) was also performed using the Scienta Omicron XPS Argus multipurpose analyser, which can be seen in Figure 21.[64] XPS was carried when the sample was loaded and after the surface was processed to see the difference in termination.

The samples were exposed to X-rays from an Al Kα X-ray source (1486.7 eV) under UHV. These X-rays excite electrons from the core levels, creating photoelectrons which can be collected and analysed for numbers and kinetic energies to provide the material they are associated with, therefore providing a useful technique to verify and identify surface termination.[65]

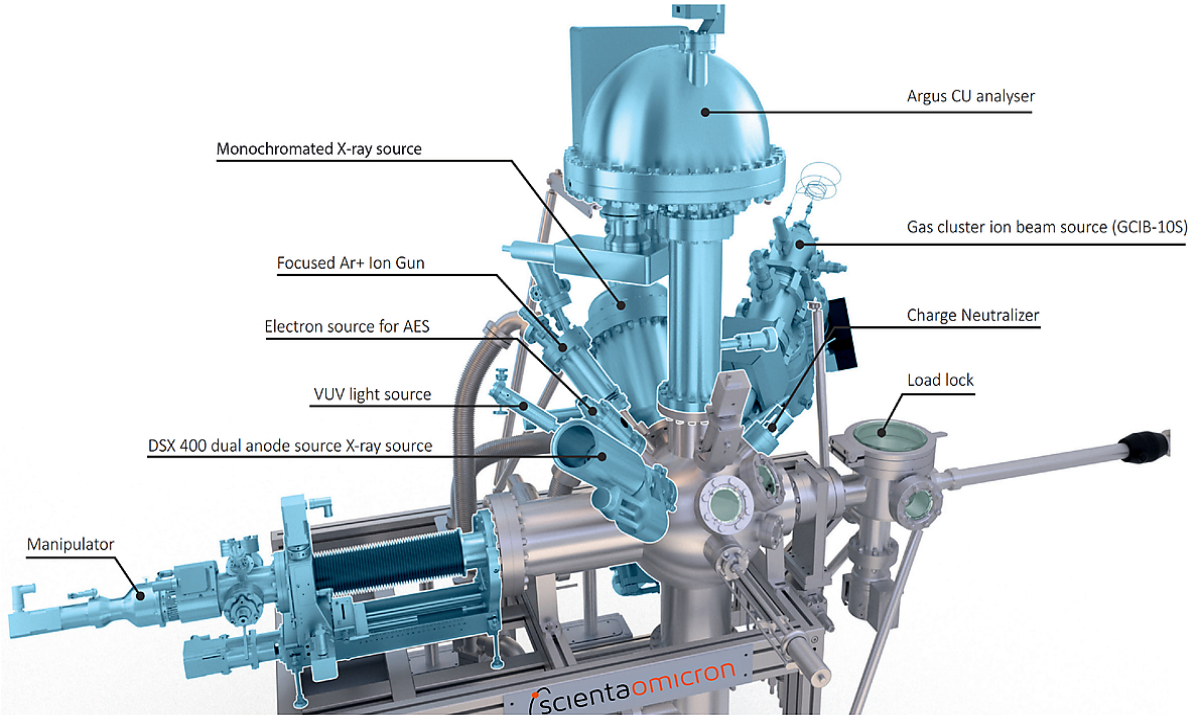

Figure 21: The Scienta Omicron XPS analyser that is found in the NanoESCA facility at the University of Bristol. This figure was taken from reference [64].

The XPS spectra were recorded with a pass energy of 50 eV and the angle between the analyser and the sample was 35°, following the procedure reported by Laverock and Fox.[66]

2.2.5 Electron Beam Characterisation

Previous dynode projects have involved analysis using the Kimble EGF-3104 electron gun powered by an EGPS-3104 power supply to characterise the gain of dynodes. The SCD dynode (Sample 3) was made in July 2025 and so it was beneficial to carry out further testing on this dynode before it was decided to modify its structure. The setup is shown in Figure 22 and the dynode was previously tested by keeping the electron gun parameters the same and varying the applied bias across the dynode (from 0 to 10 V).[51] A beam energy of 10 keV was used along with and a peak source voltage of 3 V that corresponded to a gun emission current (I_0) of approximately 2.5 mA.

The bias voltage across the dynode was increased from 0 to 20 V and the output current was measured. However, by the third repeat, the pressure inside the chamber had risen by an order of magnitude and when the sample was removed, it had warmed up which indicated charging up effects.

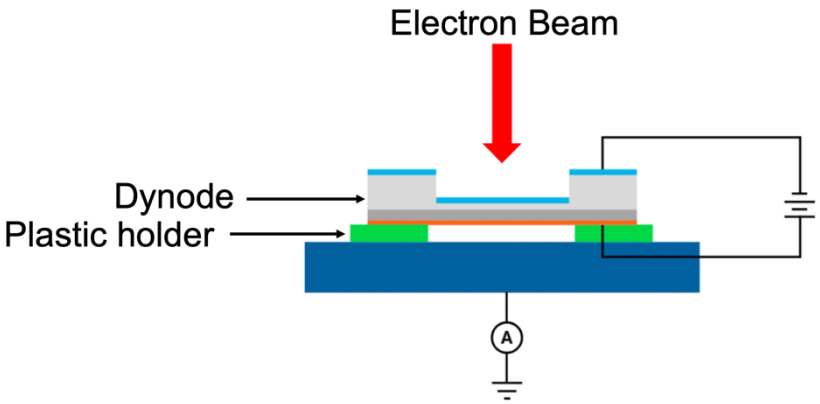

Figure 22: The experimental setup used to characterise the gain of the dynodes. Figure is taken from reference [51].

Therefore, in order to combat the charging up effects, the characterisation setup was amended to decrease the electron bombardment and saturation experienced by the dynodes.

2.2.6 Amended Setup and Method Development

To prevent charging up effects, a low efficiency photoemitter was constructed using a UV LED (wavelength of 255 nm) to irradiate a 15 nm thick gold (Au) film deposited onto quartz, as shown in Figure 23 and Figure 24. Au was chosen because of its poor photoemitting characteristics, and this meant a very low current ranging from 2.76 - 4.68 x 10^{-11} A, was emitted.

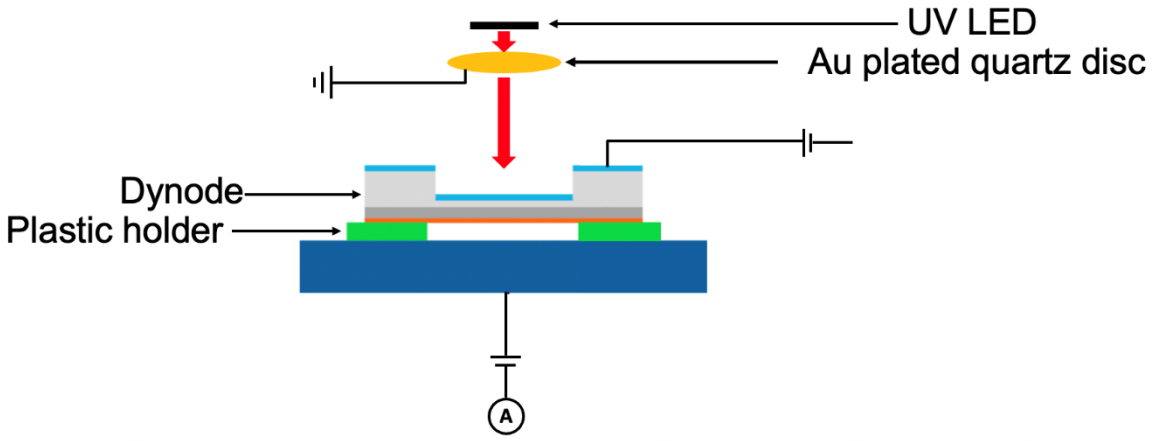

Figure 23: Updated setup to characterise the gain of the dynodes. This involved the use of a UV LED to irradiate an Au coated quartz disc. The feedthrough on the input surface of the dynode was connected to a high voltage supply unit (model PS325/2500V-25W) while the feedthrough at the anode was connected to a PLH250 DC power supply. Figure is adapted from reference [51].

This UV LED was powered by an AIM-TTI 25MHz Pulse Generator (model TGP3122) which was set to an amplitude of 6 V (with a 2.5 V offset), a frequency of 10kHz and a duty of 90 %.

Two of the four electric feedthroughs in the vacuum chamber were required for the LED alone. Therefore, only the input surface of the dynode and the anode were able to be biased. A high voltage supply unit (model PS325/2500V-25W) was used to bias the input surface of the dynode, relative to the photoemitter, from 0 to 300 V to accelerate the photoelectrons to the dynode. To collect the output from the transmission dynode, a positively biased anode plate, using PLH250 DC power

supply, was used. However, this had a maximum voltage output of 20 V so the voltage was only varied between 0 and 20 V.

The output current was measured with a Keithley 2400 source meter and 10 repeats were collected from 0 to 20 V, with one-volt increments, applied to the anode at varying voltages applied to the dynode. This was conducted in a vacuum ranging from 1.1 x 10^{-6} - 2.8 x 10^{-7} mbar and an interval of five minutes was employed between measurements, where the applied voltage to the dynode was changed, to prevent the effects of charging up.

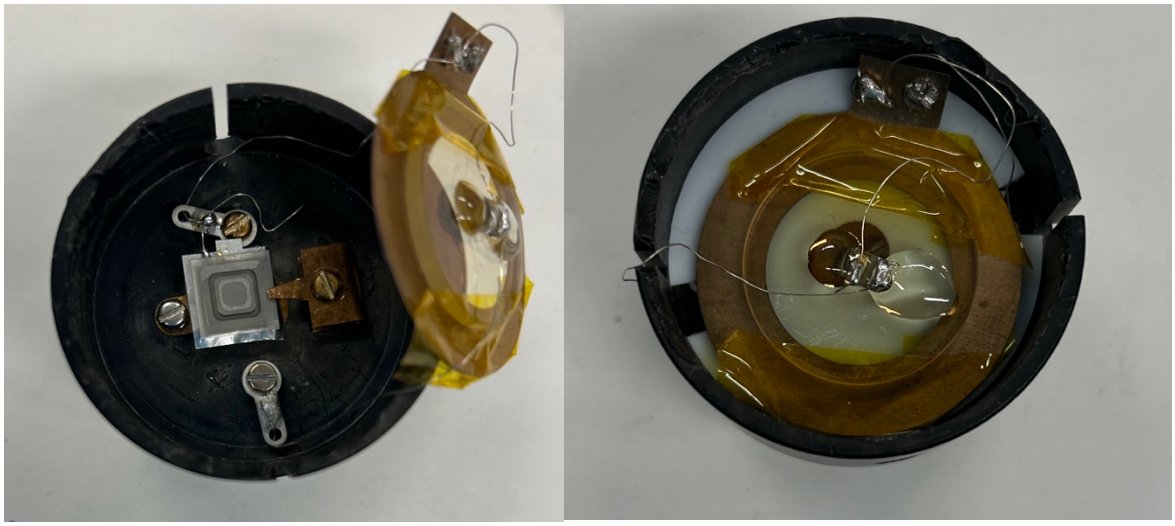

Figure 24: Configuration of the dynode and UV LED before analysis. The UV LED was attached to the Au plated quartz disc with epoxy resin.

3 Results and Discussion

3.1 Laser Micromachining of Membranes

The use of laser ablation to fabricate diamond membranes has proven to be a useful, yet difficult, process. Care had to be taken when creating these membranes as they are very prone to fracture or being burnt through, and this was much more likely as the membrane got thinner. Therefore, in order to prevent this, a process of slowly powering down the laser as the membrane became thinner was utilised. An overview of powers in conjunction with the amount of diamond removed can be found in Table 7. However, this made for quite a time-consuming process although once one sample was completed, this allowed for a better understanding of the procedure and the next samples were completed at a much faster rate. This is also shown in Table 7 where much fewer passes were needed for Sample 2 because the process was better understood.

Table 7: An overview of the laser process. This displays the power decrease as more diamond is removed. Sample 1 and 2 are PCD samples.

Sample 1			Sample 2		
Etch pass	Power / %	Thickness / µm	Etch pass	Power / %	Thickness / µm
0	0	270	0	0	320
2 x	35	215	5 x	35	180
1 x	30	195	5 x	30	60
9 x	25	85	4 x	20	30
4 x	20	55	1 x	11.5	27
3 x	15	49	1 x	10	Smoothing
3 x	12	45			(etch speed 3)
6 x	11.5	40			
2 x	11	37			
5 x	10	30			
1 x	10	Smoothing			
		(etch speed 3)			

Moreover, all membranes, both PCD and SCD, were able to reach 30 μm or less which demonstrates the repeatability of this process and while thinner membranes are likely to be achievable, this was not carried out due to the risk of fracture and for the purpose of having a sample to analyse for this project.

On the whole, laser ablation is easy to setup and run and, as shown, there are ways to avoid fracture, but it can be quite time consuming and leads to rougher surfaces. In the future, different etching processes may be worth testing for example, the use of inductively coupled plasma reactive ion etching (ICP-RIE) with O_2 or Argon (Ar) plasmas. This creates reactive ion species that can etch the surface as a result of sputtering and chemical reactions.[67] This may be useful for selective diamond patterning, where laser ablation would take a much longer time successively etching individual areas. Additionally, ion beam etching (IBE) is a great option to smooth membranes, causing them less damage.[68] However, these processes are not without their issues, for example it takes some trial and error to get the right ratios of gases for optimal etching conditions but once this is correct, it could be a useful tool for faster selective area etching of diamond.[69] Alternatively, it could be used after to laser etching, once this has removed the bulk of the diamond, to provide a smoother membrane as was utilised by Skukan *et al*.[55]

3.2 LEXT Laser Microscope Analysis

The LEXT optical microscope was very useful in monitoring the membrane process by producing height profiles. These can be seen in Figure 25 and less steps are shown for Sample 2, due to the difference in fabrication process, while the heights for all membranes are approximately 30 μm. These thin membranes will be very beneficial in achieving efficient electron transport and ensuring more secondary electrons are produced than if a thicker film was used.

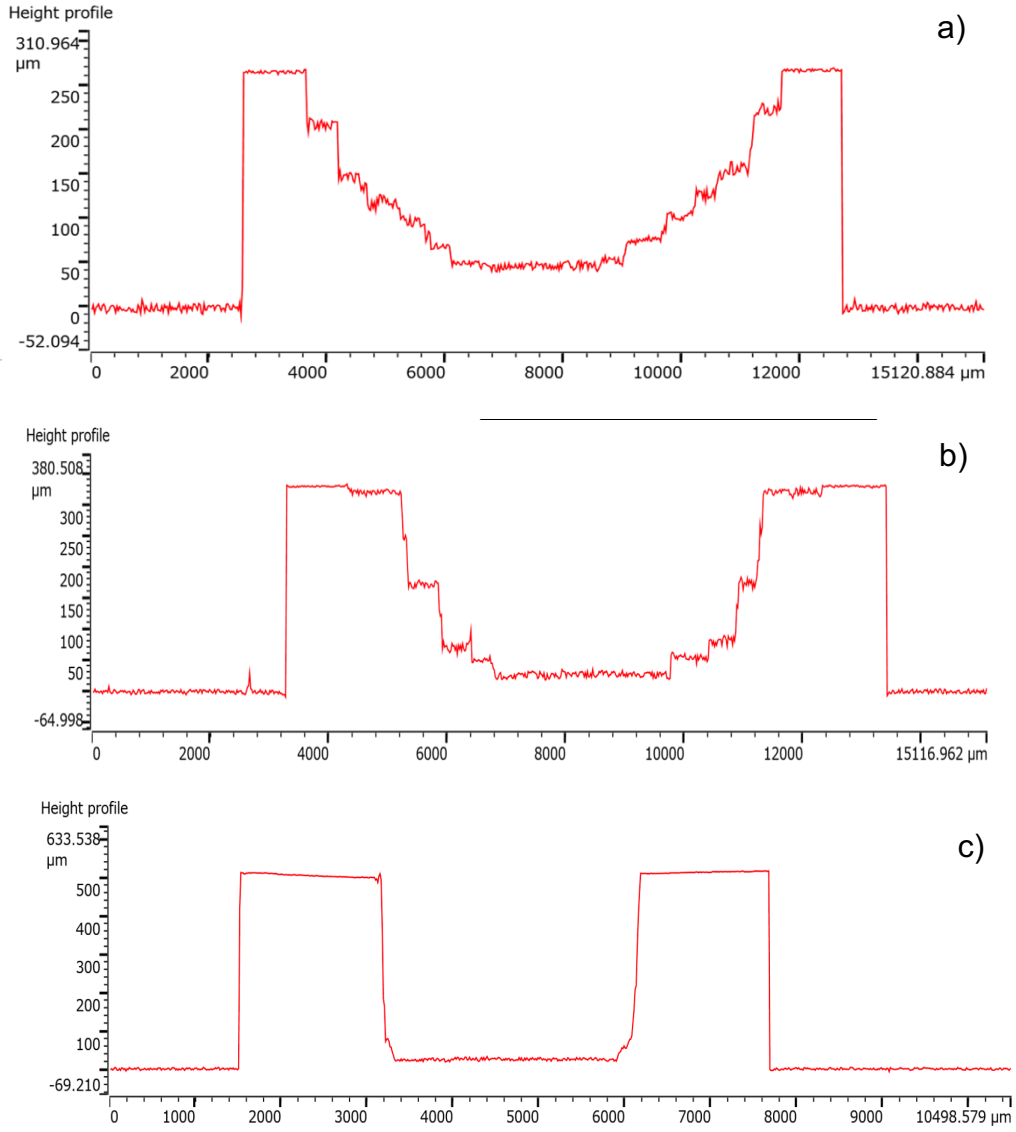

Figure 25: The height profiles of completed membranes. a) Shows the profile for Sample 1, b) shows the profile for Sample 2 and c) shows the profile for Sample 3, the SCD sample.

As well as height profiles, multiple scans can be put together (known as stitches) to provide an image of the dynode. Figure 26 shows the stiches of the samples to build a 3D image of the dynode.

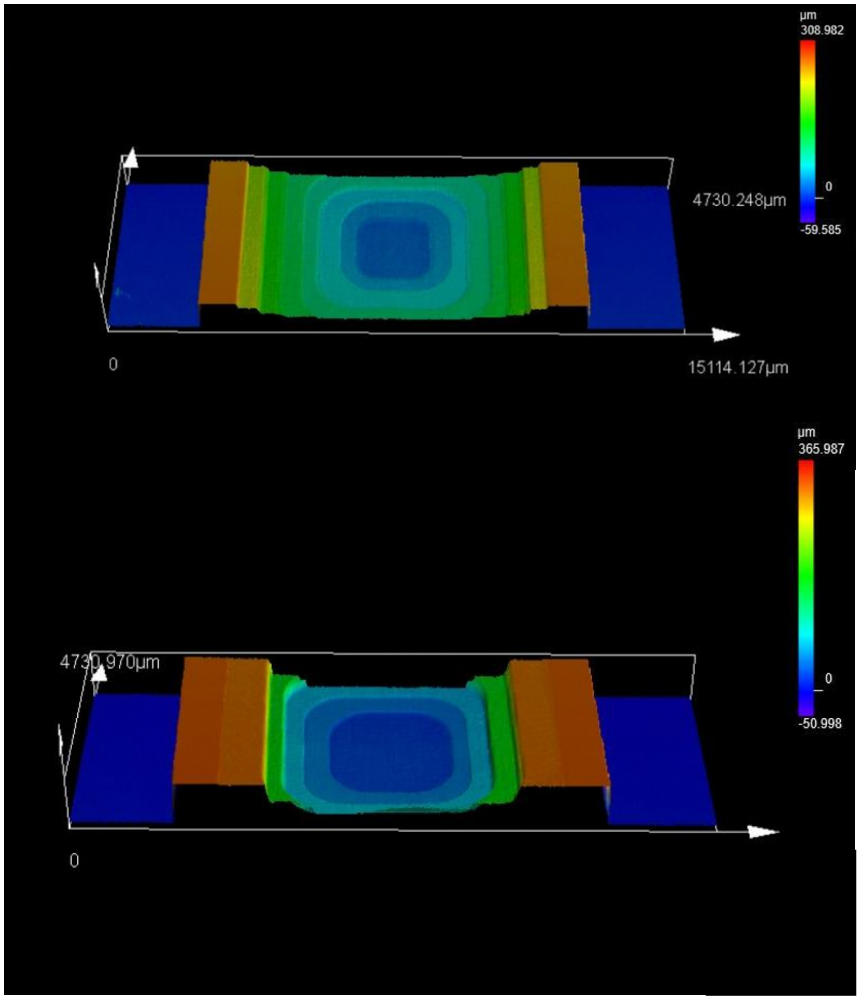

Figure 26: Stitches showing a 3D image of Sample 1 (top) and Sample 2 (bottom). These showcase the stepped membranes.

3.3 SEM Surface Analysis

Figure 27 shows SEM images of one of the PCD dynodes (Sample 1) once fabrication was complete. The images showcase the stepwise membrane which was very effective in helping to achieve a thin membrane in the centre of such a large substrate. As well as this the central 2x2 mm membrane, shown in Figure 28, displays the grains of the PCD diamond (grown on the backside of the dynode) which highlights how thin the membrane is. This is also helpful to show that that the grains stayed intact and were not damaged by the lasering process.

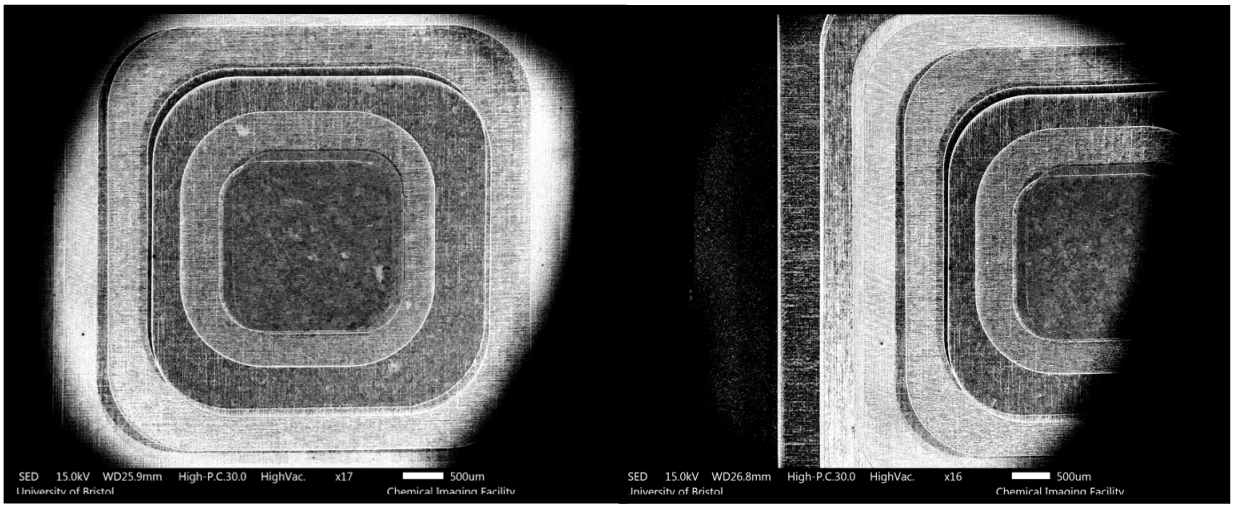

Figure 27: SEM images showing the stepwise membrane employed for the dynodes. Images taken of Sample 1.

It is worth noting from these images that the membrane template was not always perfectly aligned. This does not have a large impact on the dynode function as this does not hugely affect the central membrane, where electron multiplication will take place. In the future, this can be improved by taping the dynode to the stage of the laser cutter to avoid shifts during the process and placing it in the same direction each time.

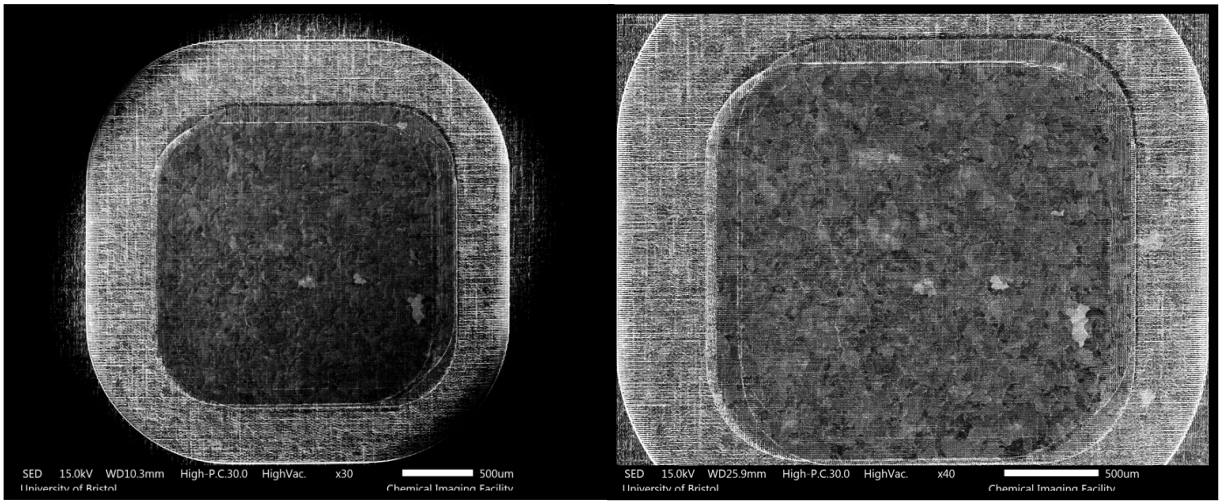

Figure 28: SEM images of the central 2x2 mm membrane, the thinnest part of the dynode. The grains of the PCD are visible and intact. Images taken of Sample 1.

Figure 29 highlights the differences between the surface roughness of the 4x4 mm and 3x3 mm membranes, where the grooves left by the laser are quite prominent, in contrast to the 2x2 mm membrane. The lines here are much less prevalent in

comparison to the others because of the smoothing processes only the 2x2 mm membrane was subjected to. Smooth surfaces are important to dynodes as this provides a uniform and efficient emission of electron. Rougher surfaces can trap or unpredictably scatter electrons, resulting in a lower gain.[70]

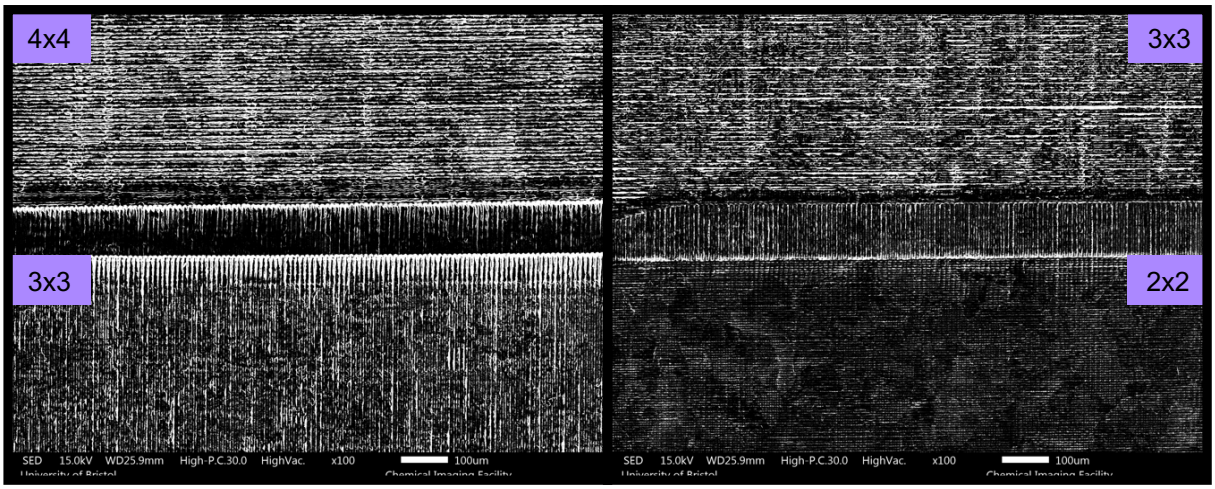

Figure 29: SEM images comparing the surfaces of different areas of the membrane. Only the 2x2 mm membrane was subjected to smoothing processes and so the grooves are less noticeable than with the 3x3 mm and 4x4 mm areas. Images taken of Sample 1.

The smoothing techniques could not be employed throughout the fabrication of the entire membrane as they were quite time consuming, and do not remove much diamond, hence they were used at the end of the fabrication process to smooth the active area that will be used for electron multiplication. This involved powering the laser down while increasing the speed to level the peaks left by the laser and provide shallower grooves. Additionally, decreasing the Z focus slightly (approximately 0.1 mm) also helped provide a more diffuse power, preventing the creation of such intense grooves and assisting the process of smoothing.

Significant improvement to smoother surfaces can be seen from the comparison of the 2x2 mm membrane to the others however, faint grooves from the laser can still be seen, although much less prominent. This may be improved by the repetition the low power passes, especially with the less focused laser, as only a few passes with this were done. However, as the membrane was quite thin already, further passes with the laser increased the risk of fracture therefore this was not carried out to a full extent so to still have a complete membrane for analysis. In the future, where there is more time,

fabrication processes can be subjected to more smoothing passes as very little diamond is removed between these passes (approximately 1 μm).

3.4 Raman Spectroscopy

Raman was carried out on the samples throughout the fabrication process, particularly after laser etching, where the femtosecond laser caused a graphitic change to the surface. Raman provided a great monitoring technique to ensure this graphitic layer was removed by the hydrogen plasma etch.

Figure 30 shows a sample directly after the laser etching. Here the graphitic peak at 1580 cm^{-1} can be seen and this is contrasted with Figure 31 which shows the same sample after being cleaned by the hydrogen plasma. It noticeably lacks a graphitic peak which is ideal to ensure the hydrogen plasma was successful in removing the graphitic debris from the laser process.[71]

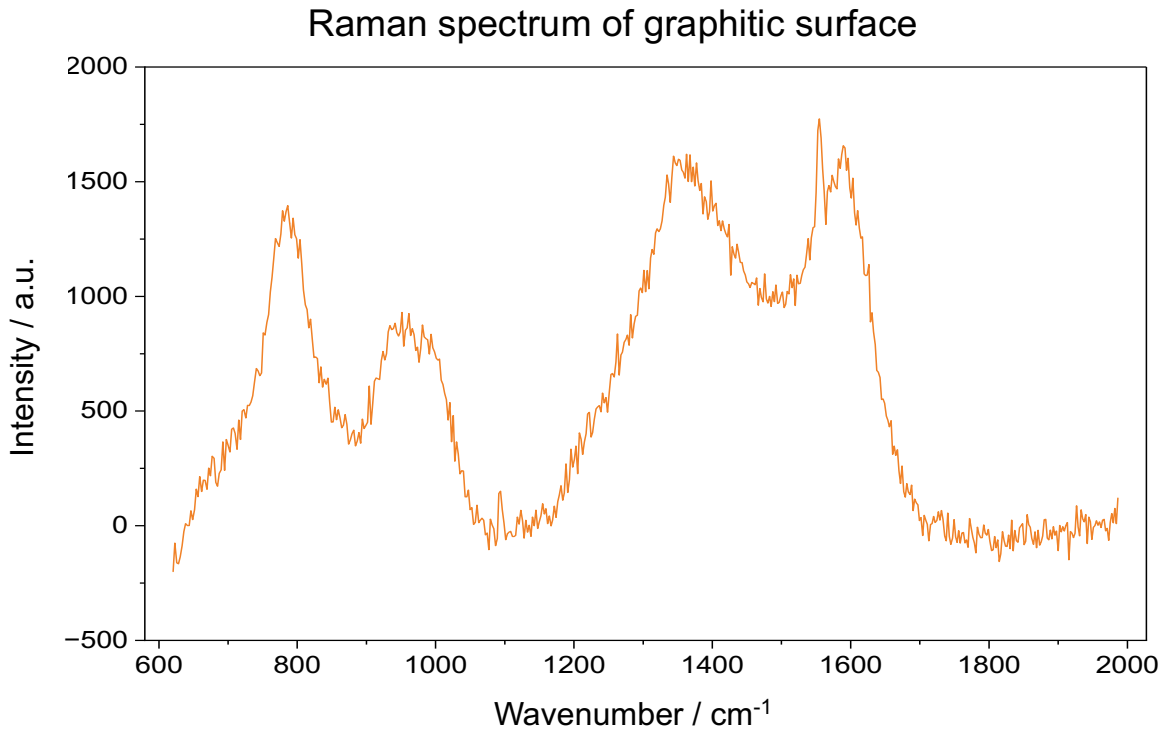

Figure 30: Raman spectrum of the graphitic surface as a result of the lasering process.

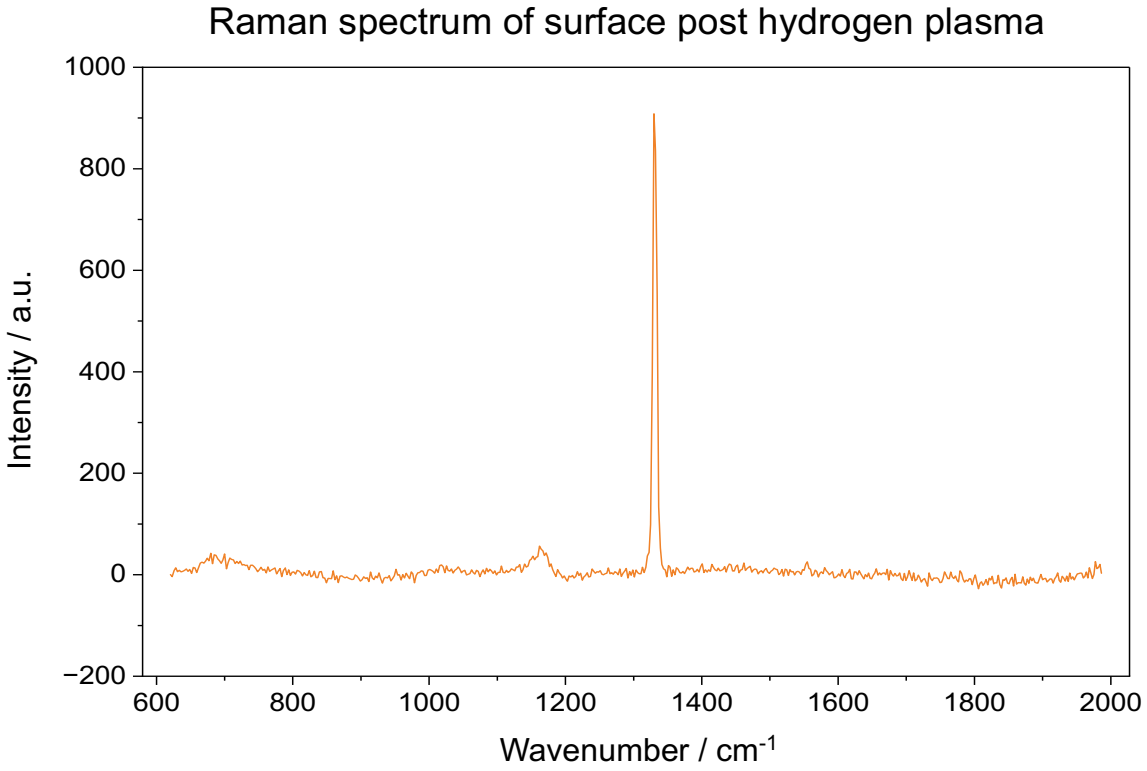

Figure 31: Raman spectrum showing the sample post hydrogen plasma treatment. This was used to etch the graphitic layer away.

The diamond peak expected at 1332 cm^{-1} is actually found at 1329 cm^{-1} which may be due to the fact this was a polycrystalline sample and the grain boundaries may affect the diamond peak. From literature, boron doping affects the Raman spectra by the inclusion of two broad, peaks at approximately 500 cm^{-1} and 1200 cm^{-1}.[72] While these samples were not as heavily doped as in some reports showing these spectra, a small, broad peak around the 1200 cm^{-1} region can be seen, with a similar intensity to that seen in literature.[73] This shows the maximum of the diamond phonon density of states (PDoS) and suggests incorporation of boron into the lattice. However, as mentioned, these Raman spectra will not fully mirror those in literature as they are not as heavily doped.

It would have been ideal to carry out a wider scan of the samples to help see the characteristic 500 cm^{-1} peak of BDD from which the Lorentzian component could be used to determine the concentration of boron doping in the diamond, by using equation 3.[74]

$$[B] / cm^{-3} = 8.44 \times 1030 \exp(-0.048\omega) \quad \text{Eq. (3)}$$

However, this was decided once the surface termination was complete, so in order to maintain the termination the plan was to carry this out after SEY testing but by this time the Raman system was moved, and therefore out of action, due to the arrival of new lab equipment. However, this can still be carried out in the future once the Raman spectrometer is back in use and it would be useful to compare boron concentrations in the samples, especially as the extent of conductivity can affect electron transport and therefore dynode performance.

3.5 XPS Analysis

XPS was carried out during the process of surface termination and serves as a great tool to analyse the quality of the termination.

The XPS results for the SCD dynode (Sample 3), displayed in Figure 32 and Table 8, show the C1s core electron binding energy (BE) has a peak at 284.9 eV which is likely due to the sp^3 carbon as well as the presence of C-O bonding. This is coupled with the O1s peak at 529.4 eV and the Li1s peak at 54.4 eV which suggests there is a presence of a Li_2O surface. These values are in line with those reported by Zulkharnay *et al*. for a C(100) surface.[75] The Li_2O surface will be ideal to provide an NEA which is required by the dynodes to produce a high SEY.

Table 8: Results of XPS analysis of the surface of the SCD dynode. The C1s, O1s and Li1s core electron binding energies are shown post anneal and after termination.

Peak	BE before termination / eV	BE after termination / eV
C1s	284.3	284.9
O1s	533.1	529.4
Li1s	N/A	54.4

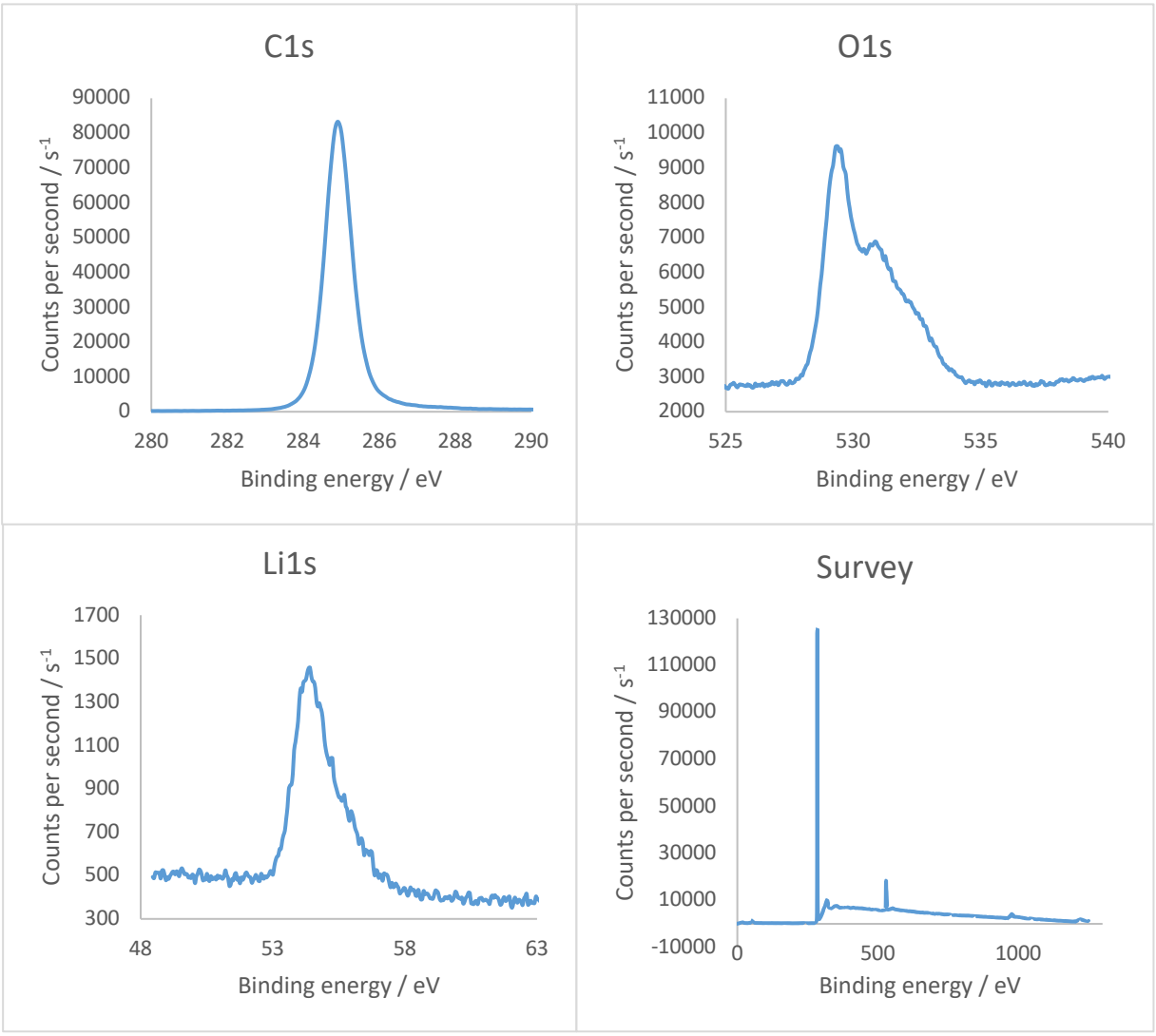

Figure 32: Results of the XPS analysis of the terminated surface of the SCD dynode. The graphs show the C1s, O1s and Li1s core electron binding energies as well as a survey spectrum.

Table 9: The results of XPS analysis of the surface of the PCD dynode. The C1s, O1s and Li1s core electron binding energies are shown post anneal and after termination.

Peak	BE before termination / eV	BE after termination / eV
C1s	284.7	284.3
O1s	532.8	533.1
Li1s	N/A	56.8

The results of the XPS analysis of the PCD sample (Sample 2) can be found in Figure 33 and Table 9. While the C1s peak has a similar BE, the others slightly vary from the SCD sample, but nicely match the work reported by Ullah *et al*. when investigating the Li-O surface of boron-doped PCD.[76] Their results also saw an O1s peak at 533.1 eV which suggests C-O bonding and as well as this they reported a Li1s peak at 56.8 eV that corresponded to ionic Li^{2+} and C-O-Li bonding. This evidence fits the XPS results of the PCD dynode surface and indicates that this sample also has a Li_2O termination.

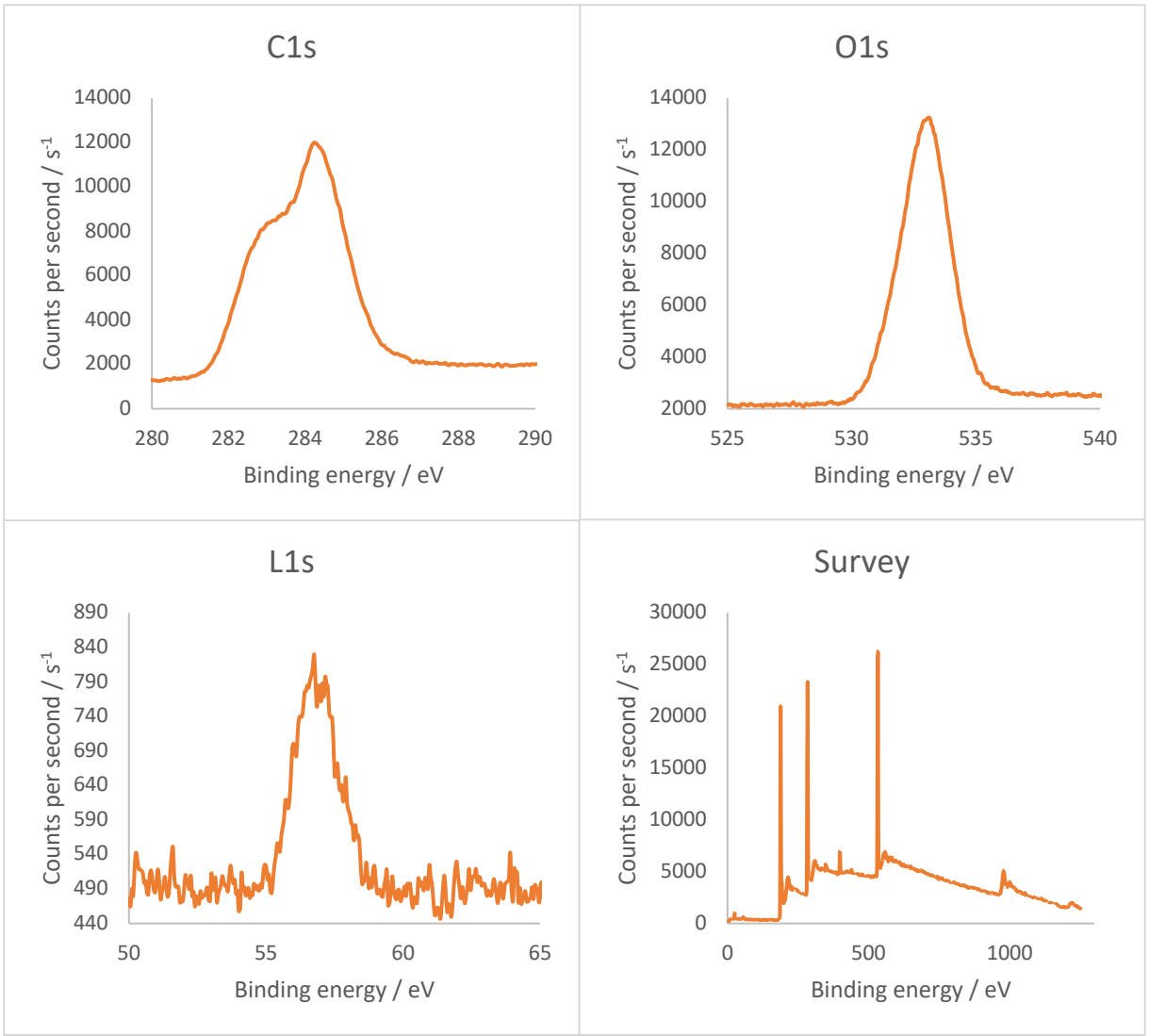

Figure 33: Results of the XPS analysis of the terminated surface of the PCD dynode. The graphs show the C1s, O1s and Li1s core electron binding energies as well as a survey spectrum.

The differences between the two samples may arise from the graphitic grain boundaries that are present in PCD diamond as well as the non-uniform surface which may interact with the X-rays differently to the ordered C(100) sample.

While the terminations of both samples should result in an NEA surface that will be beneficial to dynode function, the results from the SCD XPS may indicate a higher coverage of Li as the counts per second (CPS) for the Li1s peak was higher. This is contrasted with a noisier Li1s peak for the PCD sample which could be due to the grain boundaries present in PCD, which is also likely why the C1s peak for the PCD sample is less sharp in comparison to the SCD sample.

Alternatively, the increased noise could be because the SCD sample was more freshly hydrogen terminated before the process at the NanoESCA. This is also highlighted in the difference between the survey spectra of both samples, the PCD exhibits the presence of nitrogen at approximately 399 eV and boron at 187 eV.[77] Therefore, for future terminations, it may be beneficial to have a freshly hydrogen-terminated surface as possible before receiving Li-O treatment. However, this should not have a big impact on performance as both samples still showed the presence of a Li_2O termination.

3.6 Performance Evaluation

3.6.1 Past Analysis of the SCD Dynode

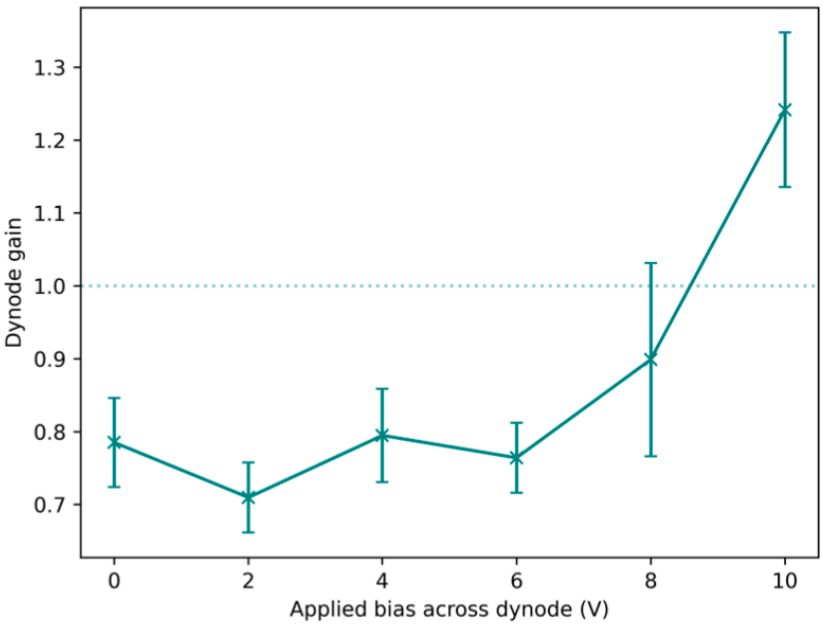

Figure 34: The results of the past SEY analysis of the SCD dynode. This was taken from reference [57].

The gain of a dynode (δ) is calculated as a ratio of the output (I_0) current to the input (I_I) current, as shown in equation 4.[78]

$$\delta = \frac{I_I}{I_0} \qquad \text{Eq. (4)}$$

The results from the previous analysis of the SCD dynode can be seen in Figure 34 and they show an increase in gain after bias of 8 V was applied, where a gain above 1 was finally seen. As the applied bias was only increased until 10 V, it was useful to carry out some more experiments, increasing this to 20 V (which was the maximum voltage output from the supplier used) to see how the dynode behaved and if the gain increased further.

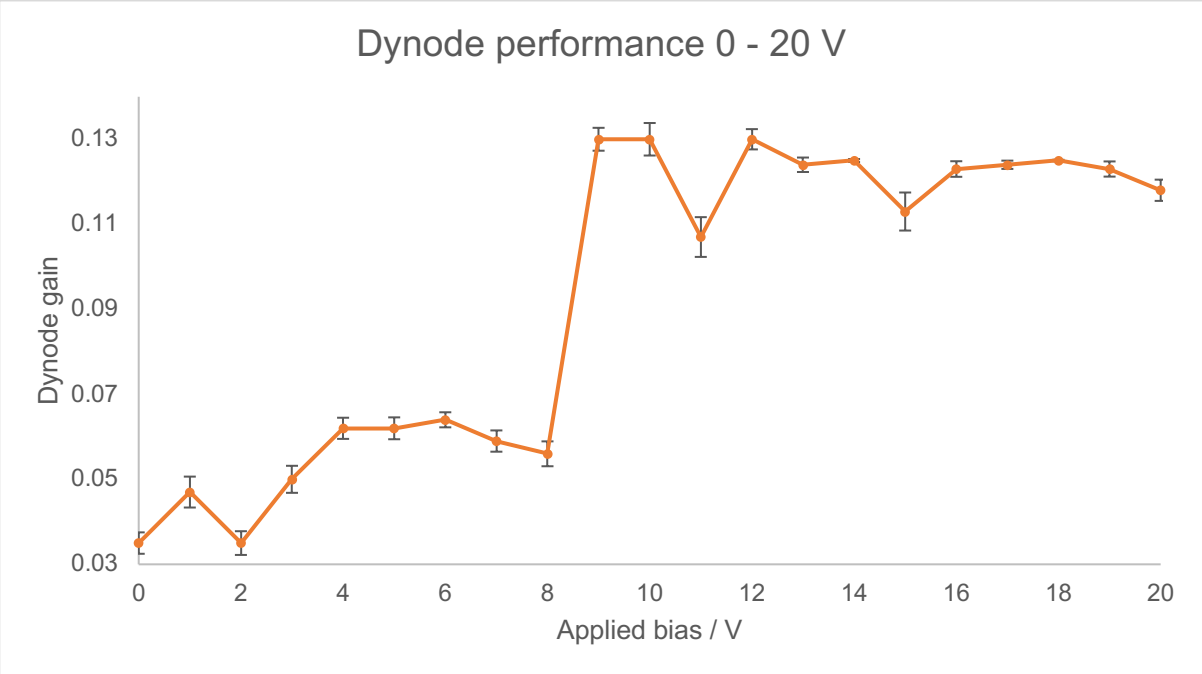

Figure 35: Results of further SEY analysis of the SCD dynode.

The results of this, shown in Figure 35, displayed the same increase in gain at an applied bias of approximately 8 V, implying that this was the amount of energy required for effective electron transport through the material. This increase is also maintained until 20 V and does not seem to be rising any further although there are some fluctuations, which may be due to a lack of repeats. The new recorded gain is much lower than the original experiments which is likely due to the degradation of the Li-O

surface termination over 3 months and the lack of an air-tight environment. Therefore, it is useful to carry out some more extensive testing on dynodes with this termination which is why the dynodes fabricated in this report were given the same surface termination. Additionally, the gain would likely be improved with a thinner membrane; these results are from a 125 μm membrane therefore, thinning this to 30 μm made it both comparable to literature and also the other dynodes in this report.

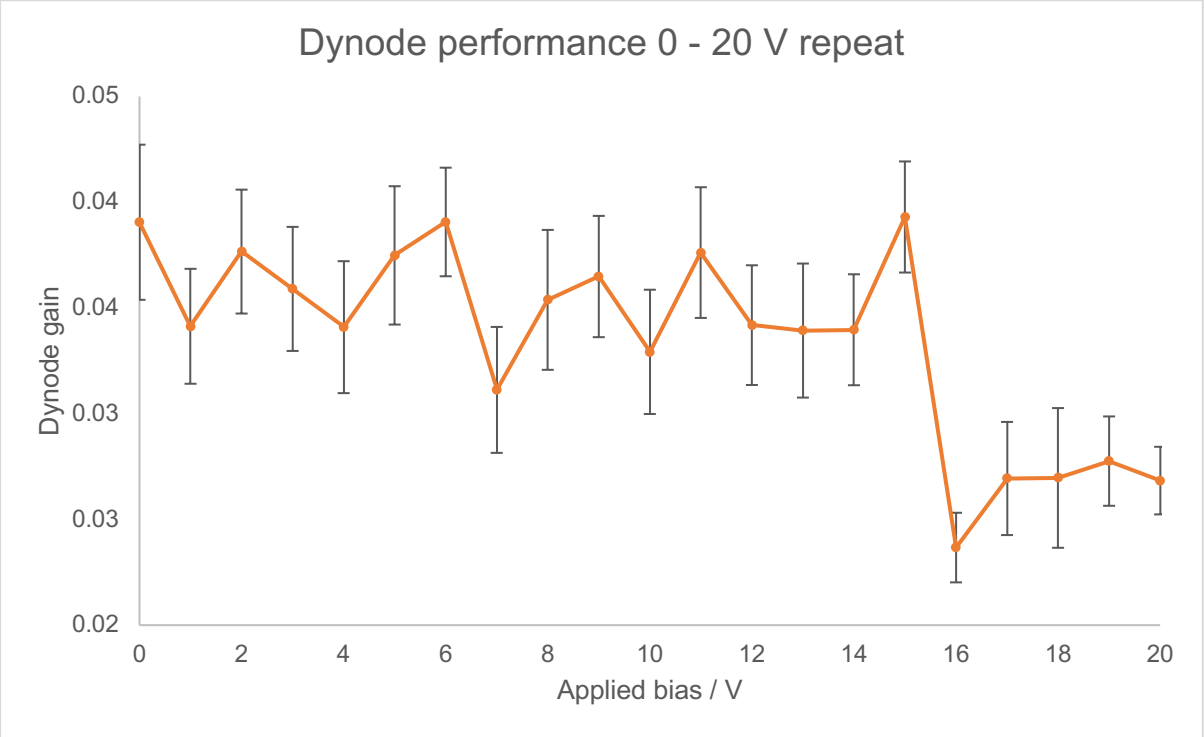

Figure 36: Graph of the repeat of the SEY analysis. This resulted in the charging up of the dynode, shown by the graph.

However, upon a repeat of this analysis which is shown in Figure 36, the graph displayed no correlation. This was accompanied by an increase in the pressure of the chamber as well as the dynode heating up. This indicates that the dynode was experiencing charging up effects which is when electrons accumulate on the dynode's surface and cannot be conducted away very well, despite it being grounded.[79] This leads to local electric fields that can alter the trajectories of incoming electrons, resulting in lower and unstable gains.[80]

This could be due to such a high bombardment of current on the dynode from the electron gun which is not beneficial when trying to gather repeats of this analysis and for real life applications, charging up cannot occur. Furthermore, when analysing dynodes in a vacuum, heated plastic (from the setup) is unideal when trying to maintain clean conditions for testing. Therefore, it is beneficial to develop improved methods to analyse these dynodes, especially as they will not be subjected to such a high current during their applications with MCP-PMTs.

3.6.2 Amended Experimental Setup

An alternative method of irradiating the transmissive diamond dynodes that produced small pulses of electrons (*ca*. 2.3 x 10^4 / pulse) was evaluated in this project. This experimental setup is much better suited to the applications of dynodes, involving use with photocathodes, and should subject the dynode to reduced primary electron irradiation and therefore hopefully less charge build-up and heating effect.

The results showed this was a much better technique to prevent charging up effects as no heating or increase in pressure was seen and more repeats were able to be collected. However, as the dynode itself was not grounded, this meant it was not immune to charging up effects and this can be seen from Figure 37 and Figure 38. Here, the highest gain was the first measurement, and it decreased with the next 19 successive measurements which is a sign the dynode was holding more charge as the testing went on. A similar effect was seen by Lapington *et al*. and was attributed to electron beam-induced contamination however, as the current emitted by this setup was so much lower, it is more likely due to charging up effects.[33]

Originally, the plan was to ground the dynode on the output surface as this is important in preventing charging up effects as well as to create a bias across the dynode. However, when this was grounded the voltage power supply would repeatedly trip out when the bias exceeded 50 V which was likely due to the formation of charge flow paths, and once the grounding was removed it was able to be biased. The formation of leakage paths was likely due to the growth of conductive BDD occurring around the edges of the dynode (the Al contact was carefully masked around the edges for this exact reason). Therefore, in the future, it may be worth completing a masked BDD

growth in the central region of the dynode to avoid these paths forming and to allow the dynode to be grounded. If grounding the dynode still results in charging up effects, then the next solution would be to incorporate a more conductive layer with a higher concentration of boron doping.

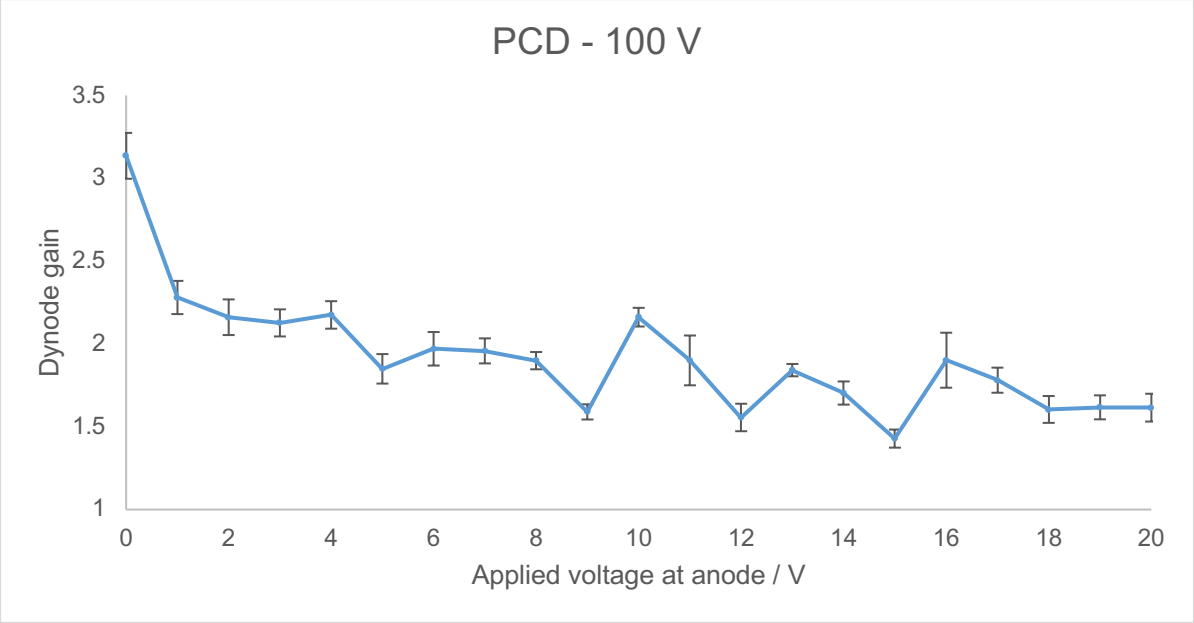

Figure 37: The gains of the PCD dynode at 100 V applied bias to the input surface. The decrease in gain indicates charging up effects.

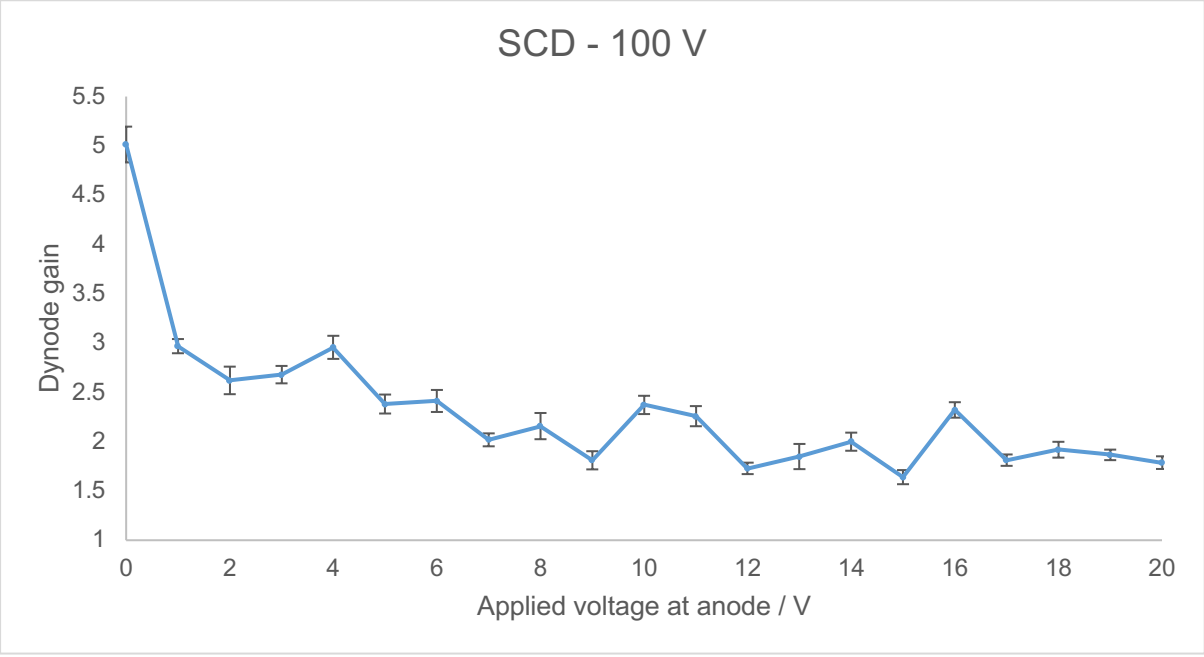

Figure 38: The gains of the SCD dynode at 100 V applied bias to the input surface. The decrease in gain indicates charging up effects.

Figure 37 and Figure 38 also show that the biasing of the anode had minimal impact on the gain. This is likely due to the fact that it could not be biased higher than the input surface of the dynode, which would create an effective accelerating gradient. Also, the slight charging up effects that were seen may have overridden the effects of the applied voltage at the anode and so also may have impacted this. Therefore, the analysis of the results will focus on the minimum and maximum gains at different applied biases of the input surface of the dynode but for future experiments, higher gains may be seen with a higher bias at the anode.

3.6.3 Analysis of Fabricated Dynodes

Despite the issues with grounding the dynodes, the results show that both dynodes were able to achieve a gain above 1, even at their lowest emitted current. This minimum gain was always towards the end of the 20 successive measurements therefore this can likely be attributed to charging up effects, but a gain was still seen despite this.

Table 10: Results of SEY analysis, using the amended setup, of the adapted SCD dynode. Results that experienced charging up are denoted with an asterisk.

Bias / V	Maximum gain	Relative u / %	Minimum gain	Relative u / %
300*	0.96	6	0.15	214
200*	0.14	80	0.11	26
100	5.01	5	1.79	5
50	3.85	4	1.86	6
15	4.29	4	2.31	5
0*	0.35	43	0.25	40

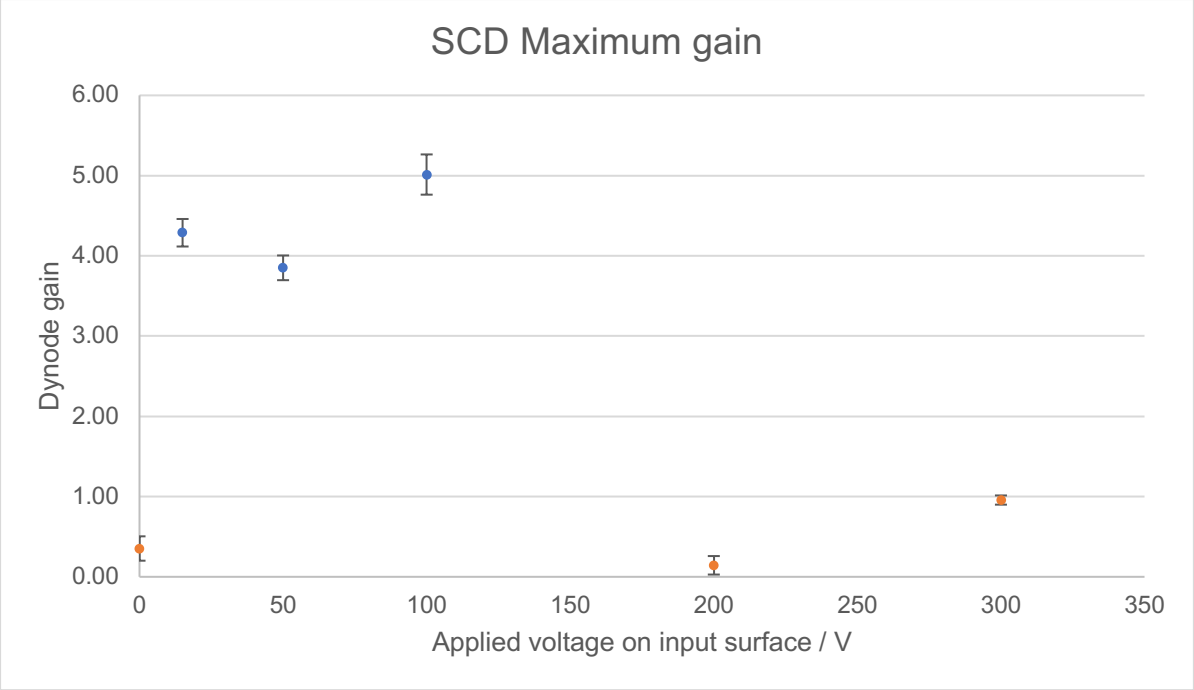

Figure 39: The maximum gain achieved by the SCD dynode. These were collected with the amended experimental setup. The results that experienced charging are shown in orange.

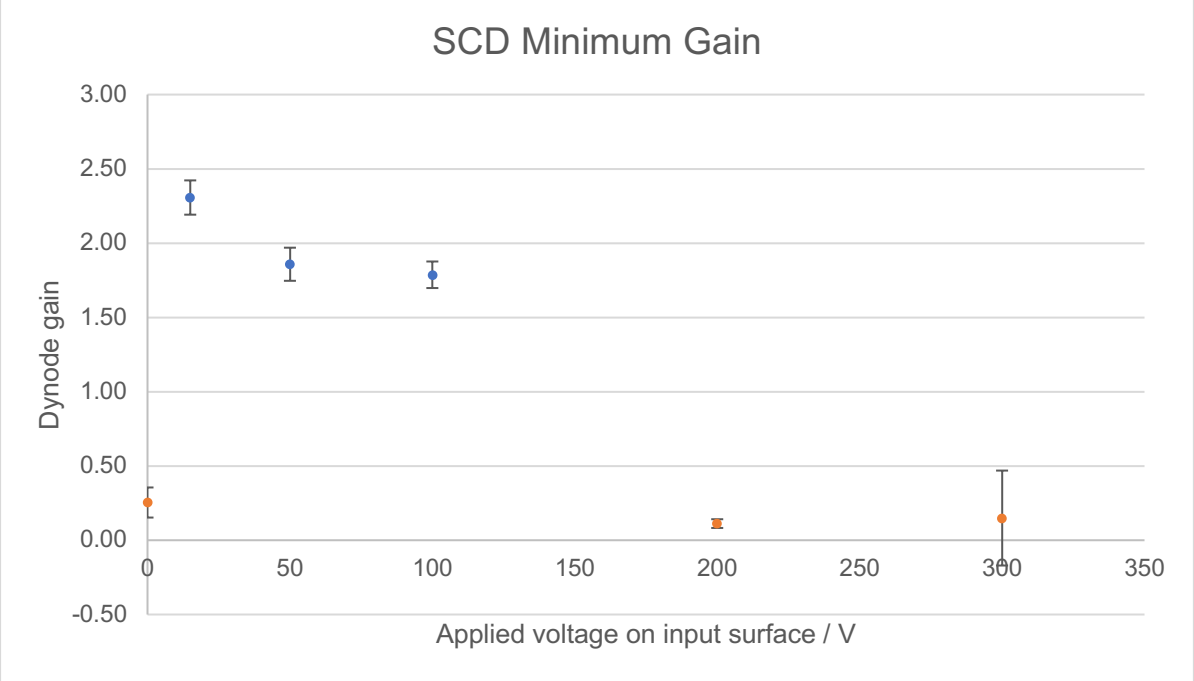

Figure 40: The minimum gain achieved by the SCD dynode. These were collected with the amended experimental setup. The results that experienced charging are shown in orange.

Overall, the SCD dynode performed better than the PCD dynode with maximum gains between 4 - 5, shown in Figure 39, and a minimum gain of approximately 2, shown in Figure 40. This is comparable to the work done by Yater *et al*. where a similar gain (3 - 4) was also recorded with a SCD dynode.[53] This is a lower gain compared to their previous work and was attributed to a lack of bias across the dynode. This may be why the SCD dynode in this report did not perform as well as those reported in literature as it did not have a bias across the dynode either, limiting the gain that can be achieved though diffusive transport alone.

Additionally, Figure 39 and Figure 40 show that the bias voltage on the input surface of the dynode had minimal effect on the gain as it did not increase with applied bias voltage. It is possible, due to the extremely fiddly nature of the experimental setup, that the electrode on the top surface did not make very good contact with the dynode therefore these effects would not be seen. Therefore, it would be beneficial to create a setup that is much easier to use and has much less margin for these errors, for example a plastic framework where the dynode could simply slot into. Although, as previously mentioned, it is possible an independent bias across the dynode (including the bottom surface) is required to see higher gains. This would have been done if there were more electric feedthroughs available, however in the future this could be introduced to improve the performance of these dynodes.

Table 11: Results of SEY analysis, using the amended setup, of the PCD dynode. Results that experienced charging up are denoted with an asterisk.

Bias / V	Maximum gain	Relative u / %	Minimum gain	Relative u / %
300	3.23	7	1.52	5
200	3.18	4	1.45	6
100	3.14	5	1.62	6
50	3.30	3	1.60	4
15*	0.69	57	0.63	35
0	3.61	4	1.59	7

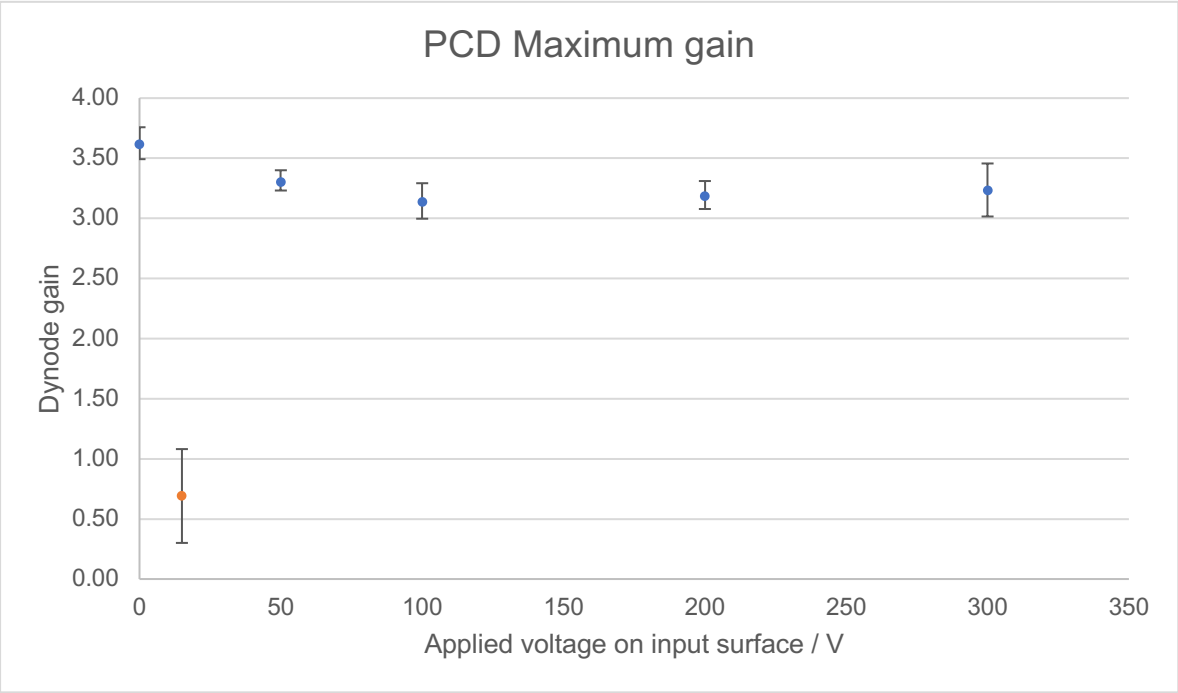

Figure 41: The maximum gain achieved by the PCD dynode. These were collected with the amended experimental setup. The results that experienced charging are shown in orange.

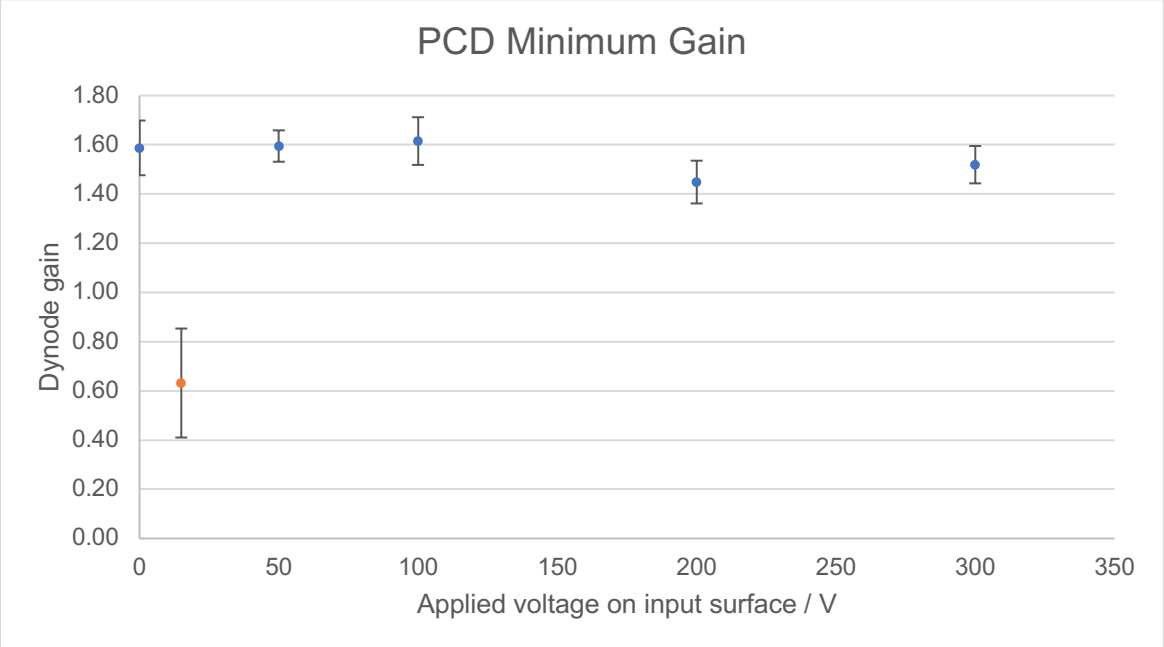

Figure 42: The minimum gain achieved by the PCD dynode. These were collected with the amended experimental setup. The results that experienced charging are shown in orange.

In contrast, the PCD dynode still achieved maximum gains of 3 - 4, shown in Figure 41, while Figure 42 shows the minimum gains achieved were between 1 and 2. This was expected as PCD includes the presence of grain boundaries and therefore increased scattering of electrons resulting in lower diffusive transport efficiency. As a result, PCD dynodes have consistently been reported as having lower gains than SCD ones, as shown in Figure 43.[27] This could also be hindered by a slightly lower coverage of Li, found by XPS analysis, which may result in a lower NEA and so lower SEY. Still, the gains found from the PCD dynode are not much lower than the SCD sample, therefore provides a more accessible option if electron multiplication is sought after but at a cheaper price.

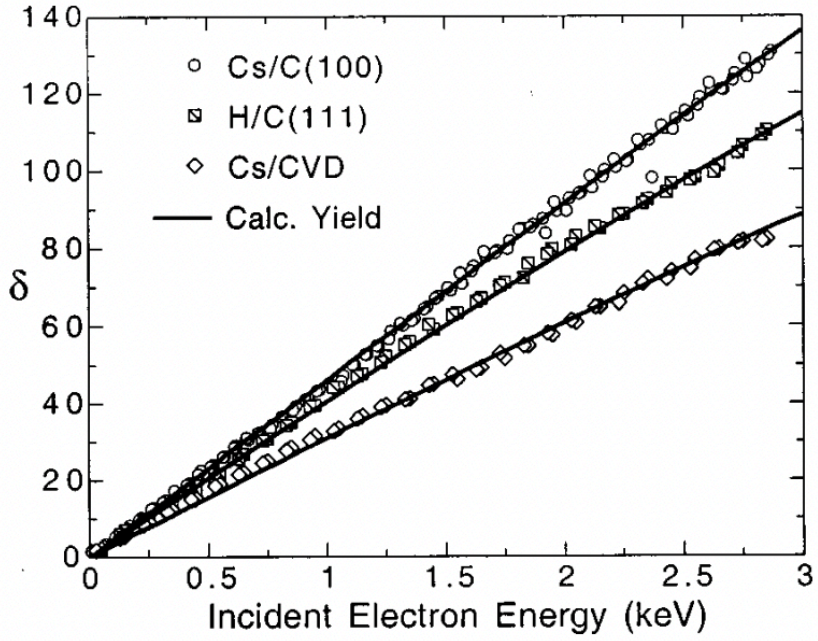

Figure 43: Shows gains reported by Yater et al. The PCD sample (labelled CVD on the graph) performs worse than the SCD samples. Figure from reference [27].

However, the PCD dynode did perform better in terms of experiencing less charging up effects. This can be seen in Table 10 and Table 11, where results with low gains (δ < 1) accompanied by a very high relative uncertainty indicate when charging up was experienced. The PCD dynode had only one of these results compared to the SCD which had three charged up results. This could be due to the size difference of the two dynodes; the PCD was a 10x10 mm dynode while the SCD was a 6x6 mm dynode. The large sample size may mean that the charge is able to dissipate easier and it also may be able to tolerate slightly more charging over a larger area. It is unclear why the

dynodes would sometimes charge up with certain bias voltages, as they were given the same break between measurements, but it could be due to a previous measurement with higher applied voltage before which requires more time to dissipate the charge. The different applied bias voltages were tested in random orders to avoid any systematic bias so this may explain why only certain results were charged ones.

As well as this, the SCD dynode was fabricated slightly differently to the PCD dynode, with the BDD on the input surface. This was carried out to investigate if more electrons could be generated in this BDD and then pulled through by the anode bias, however a higher bias on the anode was most likely required for this. Therefore, it is worth testing the SCD dynode in the reverse configuration to see if this produces a higher gain and this can easily be achieved by simply terminating the other surface. The different configuration between samples could also be affecting charging up as charge may be held on the output surface, perhaps due to the Li-O termination, which is why the PCD dynode can better tolerate this as the conductive BDD is on its output surface. This is another reason to test the SCD dynode in the same way as the PCD one as it could improve charging up and result in a more reliable gain.

To achieve higher gains with these dynodes, a few adjustments could be made. Firstly, 30 μm is quite a thin membrane however this could be made thinner to provide a higher gain, due to less material the primary electrons have to travel through. Still, higher gains have been achieved using dynodes with membranes of a similar thickness. Smedley *et al*. also fabricated a SCD dynode with a membrane thickness of approximately 30 μm.[81] Gains up to 250 were recorded, implying that the membrane thickness is sufficient and thinning it down is not necessary and particularly when considering the reproducibility of these membranes, going any thinner would make this difficult.

However, these reported gains were achieved by much higher accelerating voltages (up to 8 kV). This is consistent throughout literature, with common primary electron energies ranging from 1 - 3 keV.[27] Therefore, this suggests that much higher voltages than were used during testing are required to see a better gain with these dynodes. For example, by looking at Figure 43, an approximate bias of 500 - 300 V resulted in gains between 3 and 10 which is comparable to those reported in this project.

Therefore, increasing the accelerating voltage could result in higher gains, similar to those reported. Of course, the terminations used (H and Cs in these cases) would also affect the NEA of the surface and therefore the SEY therefore these also may be worth investigating further.

As well as this, although the distance travelled by secondary electrons was kept to a minimum (approximately 5 mm) to help produce high gains, reported experimental setups that achieved higher gains suggest this needs to be reduced. Typical distances range from 500 μm to 0.1 μm which is over 10 times smaller than the setup that was tested.[82] This could be achieved with an improved arrangement, involving a much thinner plastic spacer between the dynode and anode.

3.6.4 Uncertainty Calculations

The uncertainty for the results of SEY analysis was calculated by finding the standard error of the mean (SEM) of the results, each with 10 repeats per applied bias. This is then combined with the SEM of the control to give an uncertainty, an example of this can be found in Table 12. The SEM does provide a slight overestimation in the uncertainty, but it is still helpful to assess the results. A more accurate uncertainty could be found using the contributions from the equipment, for example the Keithley source meters, however the highest contribution is likely from the analytical result therefore this is a good indication on the uncertainty of the results.

Table 12: Uncertainty calculations corresponding to the results in Figure 40.

Bias / V	Current / pA	SEM / pA	Relative u / %	Control current / pA	Control SEM / pA	Relative u / %	Combined u / %
300	3.13	6.70	214	43.1	2.17	5	214
200	5.02	1.29	26	43.1	2.17	5	26
100	80.1	1.28	2	43.1	2.17	5	5
50	83.2	3.30	4	43.1	2.17	5	6
15	90.0	1.83	2	43.1	2.17	5	5
0	11.4	4.54	40	43.1	2.17	5	40

4 Conclusions and Future Work

This thesis aimed to present the fabrication of a transmissive diamond dynode for the purpose of creating an electron multiplication device. Two dynodes were successfully fabricated, one PCD and one SCD, and both possessed a membrane that was at most 30 μm which was able to be confirmed by LEXT laser microscope analysis. This was achieved through laser ablation which was successful in creating a thinned area; through the process of powering down the laser and the utilisation of a stepwise membrane, this was completed without experiencing any fractures. Additionally, smoothing techniques utilising the laser were beneficial in achieving more even surfaces, as was seen through the SEM analysis of the membrane. Although improved surfaces were able to be seen, this could be further improved through the use of different etching techniques such as ICP-RIE or IBE. This could also be used for selective patterning of the diamond in the future, where laser etching would be quite time consuming.

Both dynodes were able to achieve a gain above one, even at the lower end of the results, meaning electron multiplication was occurring. The SCD dynode gave maximum gains between 4 and 5 which is in line with values reported by Yater *et al*. and suggests performance would benefit from an independent bias across the dynode. A slightly lower gain was seen for the PCD at 3 - 4 but this was expected as the grain boundaries cause more electron scattering and hinders electron transport. Still, it is positive to see a gain with a PCD dynode and this may provide a cheaper alternative to SCD if a slightly lower gain is acceptable.

The gains of the dynodes could potentially be improved by further amendments to the testing process. For example, a setup that involves a framework, and therefore an easier insertion of the dynode, can help to ensure good contact is made to any electrode that may be biasing the material. This can also be used to ensure there is a very minimal distance travelled by secondary electrons (< 500 μm) which could help improve the gain. Furthermore, it is clear that accelerating voltage is also important for dynode function, so it is worth testing the dynodes with much higher voltages (> 1kV) in future experiments. As well as this, a higher voltage at the anode could help to further accelerate electrons and also result in a higher gain. All of these improvements

to the analysis process would be beneficial to carry out, perhaps in a future project, to see their effect on dynode performance and find out if a higher gain is achievable.

Moreover, both dynodes benefitted from the improved, novel setup, utilising a UV LED to irradiate gold and emit a much lower current than the electron gun used in previous analysis. This better simulated the effects of a photocathode to prevent charging up. The results showed some success in improving the repeatability and withstanding the effects of charging up but if the dynode was able to be grounded, this could be improved further. To ensure the dynodes can be grounded it may be worth carrying out a masked BDD growth to prevent charge flow paths forming around the edges. Additionally, the results suggest larger dynodes may be better at withstanding the effects of charging up as they are able to dissipate the charge more effectively. This is useful to consider for future fabrication processes and as well as this, there is possible benefit of growing the BDD on the output surface, preventing charge building up by conducting it away. This is also a reason to test the SCD dynode with the BDD on the output, as opposed to the input surface, as a more reliable gain could be recorded. If charging up is still seen, the boron doping may need to be increased and the use of wider Raman scans (400 cm^{-1} - 2000 cm^{-1}) can be used to evaluate boron concentrations.

Once the experimental setup is improved, the testing process is fully developed and dynode performance is established, future work may involve the fabrication of a dynode with a larger membrane area. This was originally intended to be carried out with Sample 2, before Sample 1 experienced a fracture, but this could result in an even higher gain as there is a larger area where effective electron transport could take place, resulting in more secondary electrons.

While a fairly good gain was achieved with the Li-O termination, for future testing a more robust surface termination, such as Sc-O, could be used.[21] This is because the results show that the lack of storage under an inert atmosphere, over a period of three months, results in a degraded Li-O termination.

Finally, in terms of real-world applications, both dynodes were able to achieve gains that would be useful for purposes of electron multiplication, while the physical insertion

into an MCP-PMT setup should work to extend lifetimes of photocathodes. They are held back by the slight charging up effects which prevents consistent use and affects repeatability. Through further amendments to the experimental setup and a better knowledge of the fabrication process, these could hopefully be negated and a fully functioning transmissive diamond dynode with higher gains could be made, resulting in more robust operation and faster response times.

5 References

1. C. Pisarciuc, *Nonconventional Technologies Review*, 2012, **XVI**, 13-18.
2. D. Das, in *Carbon-Based Nanofillers and Their Rubber Nanocomposites*, eds. S. Yaragalla, R. Mishra, S. Thomas, N. Kalarikkal and H. J. Maria, Elsevier, 2019, pp. 123-181.
3. F. Zhao, Y. He, B. Huang, T. Zhang and H. Zhu, *Materials*, 2024, **17**, 3437.
4. Y. Yamamoto, T. Imai, K. Tanabe, T. Tsuno, Y. Kumazawa and N. Fujimori, *Diamond and Related Materials*, 1997, **6**, 1057-1061.
5. R. Zulkharnay and P. W. May, *Functional Diamond*, 2024, **4**, 2410160.
6. *Crystal Research and Technology*, 1993, **28**, 602-602.
7. Y. N. Pal'yanov, A. G. Sokol, Y. M. Borzdov, A. F. Khokhryakov and N. V. Sobolev, *Nature*, 1999, **400**, 417-418.
8. U. Dhaenens-Johansson, J. Butler and A. Katrusha, *Reviews in Mineralogy and Geochemistry*, 2022, **88**, 689-753.
9. P. W. May, *Philosophical Transactions of the Royal Society A: Mathematical, Physical and Engineering Sciences*, 2000, **358**, 473-495.
10. P. W. May and R. Zulkharnay, *Philosophical Transactions of the Royal Society A: Mathematical, Physical and Engineering Sciences*, 2025, **383**, 20230382.
11. Z. Sun, B. Cui, P. Liang, Q. Liu, N. Gao and H. Li, *Diamond and Related Materials*, 2024, **141**, 110565.
12. M. C. James, F. Fogarty, R. Zulkharnay, N. A. Fox and P. W. May, *Carbon*, 2021, **171**, 532-550.
13. K. O'Donnell, T. Martin, M. Edmonds, A. Tadich, L. Thomsen, J. Ristein, C. Pakes, N. Fox and L. Ley, *physica status solidi (a)*, 2014, **211**.
14. J. B. Cui, J. Ristein and L. Ley, *Physical Review Letters*, 1998, **81**, 429-432.
15. F. Maier, J. Ristein and L. Ley, *Physical Review B*, 2001, **64**, 165411.
16. K. M. O'Donnell, T. L. Martin, N. A. Fox and D. Cherns, *Physical Review B*, 2010, **82**, 115303.
17. K. M. O'Donnell, M. T. Edmonds, J. Ristein, A. Tadich, L. Thomsen, Q.-H. Wu, C. I. Pakes and L. Ley, *Advanced Functional Materials*, 2013, **23**, 5608-5614.
18. K. M. O'Donnell, T. L. Martin and N. L. Allan, *Chemistry of Materials*, 2015, **27**, 1306-1315.
19. L. T. Martin, PhD Thesis, University of Bristol, 2011.
20. R. Zulkharnay, N. L. Allan and P. W. May, *Carbon*, 2022, **196**, 176-185.
21. R. Zulkharnay, N. A. Fox and P. W. May, *Small*, 2024, **20**, 2405408.
22. K. M. O'Donnell, M. T. Edmonds, A. Tadich, L. Thomsen, A. Stacey, A. Schenk, C. I. Pakes and L. Ley, *Physical Review B*, 2015, **92**, 035303.
23. R. Vaz, P. W. May, N. Fox, C. J. Harwood, V. Chatterjee, J. Smith, C. Horsfield and S. Osbourne, *Journal of Instrumentation*, 2015, **10**.
24. A. Shih, J. Yater, C. Hor and R. Abrams, *Applied Surface Science*, 1997, **111**, 251-258.
25. R. Tappert and M. C. Tappert, in *Diamonds in Nature: A Guide to Rough Diamonds*, eds. R. Tappert and M. C. Tappert, Springer Berlin Heidelberg, Berlin, Heidelberg, 2011, pp. 13-42.
26. S. Goel, X. Luo, A. Agrawal and R. L. Reuben, *International Journal of Machine Tools and Manufacture*, 2015, **88**, 131-164.
27. J. E. Yater and A. Shih, *Journal of Applied Physics*, 2000, **87**, 8103-8112.
28. B. L. Mackey, J. N. Russell, J. E. Crowell, P. E. Pehrsson, B. D. Thoms and J. E. Butler, *The Journal of Physical Chemistry B*, 2001, **105**, 3803-3812.

29. G. Alba, M. P. Villar, R. Alcántara, J. Navas and D. Araujo, *Journal*, 2020, **10**, 1193.
30. H. Gomez, M. N. Groves and M. R. Neupane, *Carbon Trends*, 2021, **3**, 100033.
31. D. Vázquez-Cortés, S. D. Janssens and E. Fried, *Carbon*, 2024, **228**, 119298.
32. P. P. Filippatos and A. Chroneos, *Journal of Applied Physics*, 2025, **138**, 030702.
33. J. S. Lapington, D. P. Thompson, P. W. May, N. A. Fox, J. Howorth, J. Milnes and V. Taillandier, *Nuclear Instruments and Methods in Physics Research Section A: Accelerators, Spectrometers, Detectors and Associated Equipment*, 2009, **610**, 253-257.
34. J. Miller and G. Brandes, *Journal of Applied Physics*, 1997, **82**, 4538-4545.
35. J. A. Holcombe, in *Encyclopedia of Analytical Science (Second Edition)*, eds. P. Worsfold, A. Townshend and C. Poole, Elsevier, Oxford, 2005, pp. 249-258.
36. MCP-PMT Series, https://penlink.se/product/mcp-pmt/, (accessed April 2026).
37. DETECTORS: Diamond dynodes create new breed of photon detectors, https://www.laserfocusworld.com/detectors-imaging/article/16563275/detectors-diamond-dynodes-create-new-breed-of-photon-detectors, (accessed January 2026).
38. P. R. Bolton, M. Borghesi, C. Brenner, D. C. Carroll, C. De Martinis, F. Fiorini, A. Flacco, V. Floquet, J. Fuchs, P. Gallegos, D. Giove, J. S. Green, S. Green, B. Jones, D. Kirby, P. McKenna, D. Neely, F. Nuesslin, R. Prasad, S. Reinhardt, M. Roth, U. Schramm, G. G. Scott, S. Ter-Avetisyan, M. Tolley, G. Turchetti and J. J. Wilkens, *Physica Medica*, 2014, **30**, 255-270.
39. E. J. Baldwin, J. S. Lapington and S. A. Leach, *Nuclear Instruments and Methods in Physics Research Section A: Accelerators, Spectrometers, Detectors and Associated Equipment*, 2025, **1070**, 170038.
40. A. Lehmann, M. Böhm, D. Miehling, M. Pfaffinger, S. Stelter, F. Uhlig, A. Ali, A. Belias, R. Dzhygadlo, A. Gerhardt, M. Krebs, D. Lehmann, K. Peters, G. Schepers, C. Schwarz, J. Schwiening, M. Traxler, L. Schmitt, M. Düren, E. Etzelmüller, K. Föhl, A. Hayrapetyan, K. Kreutzfeld, J. Rieke, M. Schmidt, T. Wasem and C. Sfienti, *Nuclear Instruments and Methods in Physics Research Section A: Accelerators, Spectrometers, Detectors and Associated Equipment*, 2020, **952**, 161821.
41. L. Ma, G. Huang, Z. Hua, M. Jin, Z. Jin, S. Liu, S. Qian, L. Ren, S. Si, J. Sun, Q. Wu, X. Wang, Y. Wang, Z. Wang, Z. Wang, N. Wang, K. Wu, M. Yan, H. Zhang and Y. Zhu, *Nuclear Instruments and Methods in Physics Research Section A: Accelerators, Spectrometers, Detectors and Associated Equipment*, 2022, **1041**, 167333.
42. X. Zhou, J. Bec, D. Yankelevich and L. Marcu, *Optics Express*, 2021, **29**, 20105-20120.
43. G. F. Trindade, S. Sul, J. Kim, R. Havelund, A. Eyres, S. Park, Y. Shin, H. J. Bae, Y. M. Sung, L. Matjacic, Y. Jung, J. Won, W. S. Jeon, H. Choi, H. S. Lee, J.-C. Lee, J.-H. Kim and I. S. Gilmore, *Nature Communications*, 2023, **14**, 8066.
44. L. Chen, X. Wang, J. He, L. Tian, J. Tian, Q. Wang, Y. Wang, J. Yang, J. Qian and F. Zhang, *Scientific Reports*, 2022, **12**, 10445.
45. F. Gao, S. Qian, A. Sidorenkov and B. Lubsandorzhiev, *The Innovation*, 2026, **7**, 101263.

46. Q. Peng, W.-S. Choong and W. Moses, *IEEE transactions on nuclear science*, 2013, **60**, 3212-3219.
47. A. S. Tremsin and J. V. Vallerga, *Radiation Measurements*, 2020, **130**, 106228.
48. A. Lehmann, A. Britting, W. Eyrich, M. Pfaffinger, F. Uhlig, A. Belias, R. Dzhygadlo, A. Gerhardt, K. Götzen, G. Kalicy, M. Krebs, D. Lehmann, F. Nerling, M. Patsyuk, K. Peters, G. Schepers, L. Schmitt, C. Schwarz, J. Schwiening, M. Traxler, M. Zühlsdorf, M. Düren, E. Etzelmüller, K. Föhl, A. Hayrapetyan, B. Kröck, O. Merle, J. Rieke, M. Schmidt, E. Cowie, T. Keri, P. Achenbach, M. Cardinali, M. Hoek, W. Lauth, S. Schlimme, C. Sfienti and M. Thiel, *Nuclear Instruments and Methods in Physics Research Section A: Accelerators, Spectrometers, Detectors and Associated Equipment*, 2017, **845**, 570-574.
49. D. R. Beaulieu, D. Gorelikov, P. de Rouffignac, K. Saadatmand, K. Stenton, N. Sullivan and A. S. Tremsin, *Nuclear Instruments and Methods in Physics Research Section A: Accelerators, Spectrometers, Detectors and Associated Equipment*, 2009, **607**, 81-84.
50. E. V. Antamanova, I. G. Bearden, E. J. Garcia-Solis, A. V. Harton, V. A. Kaplin, T. L. Karavicheva, J. L. Klay, Y. A. Melikyan, D. V. Serebryakov, M. Slupecki and W. H. Trzaska, *Journal of Instrumentation*, 2018, **13**, T09001.
51. H. Qiu, Universilty of Bristol, 2025.
52. S. Tao, H. Chan and H. Graaf, *Materials*, 2016, **9**.
53. J. E. Yater, J. L. Shaw, K. L. Jensen, T. Feygelson, R. E. Myers, B. B. Pate and J. E. Butler, *Diamond and Related Materials*, 2011, **20**, 798-802.
54. J. S. Lapington, V. Taillandier, B. L. Cann, J. Howorth, J. Milnes, R. Vaz, P. W. May, N. A. Fox, R. Stevens and L. Wang, *Journal of instrumentation*, 2012, **7**, E04002.
55. N. Skukan, V. Grilj, I. Sudić, M. Pomorski, W. Kada, T. Makino, Y. Kambayashi, Y. Andoh, S. Onoda, S. Sato, T. Ohshima, T. Kamiya and M. Jakšić, *Applied Physics Letters*, 2016, **109**, 043502.
56. S. M. Leeds, PhD Thesis, University of Bristol, 1999.
57. Y. Lian, Z. Zhang, M. Liang, X. Zhao, K. Guo, J. Li, Z. Li and Y. Lu, *Applied Physics Letters*, 2026, **128**, 081603.
58. Principles of Laser Scanning Microscopes, https://evidentscientific.com/en/learn/knowledge/metrology/lext-principles/basic, (accessed April 2026).
59. Confocal Laser Scanning Microscopy Explained In 3 Easy Steps, https://bitesizebio.com/19958/confocal-laser-scanning-microscopy/, (accessed April 2026).
60. M. Tare, O. Puli, S. Oros and A. Singh, *Population Data Information Service*, 2009, **92**, 174-180.
61. Scanning Electron Microscopes (SEM), https://www.jeol.com/products/science/sem.php, (accessed April 2026).
62. A. A. Bunaciu and H. Aboul-Enein, *Critical reviews in analytical chemistry*, 2016, **47**.
63. Multiple lasers and gratings for Raman and PL spectroscopy, https://www.renishaw.com/cs/multiple-lasers-and-gratings-for-raman-and-pl-spectroscopy--25938?srsltid=AfmBOorpXko1eKbjBMm5Q9bRrti7HY4vmQIc4sYt9drtIgEbNjJwPm6O, (accessed April 2026).

64. XPS Lab, https://scientaomicron.com/en/products-solutions/electron-spectroscopy/XPS-Lab, (accessed April 2026).
65. X-Ray Photoelectron Spectroscopy (XPS), https://scientaomicron.com/en/products-solutions/electron-spectroscopy/XPS-Lab/technology/XPS/40, (accessed April 2026).
66. J. Laverock and N. A. Fox, *Surface and Interface Analysis*, 2026, **n/a**.
67. I. Bello, M. K. Fung, W. J. Zhang, K. H. Lai, Y. M. Wang, Z. F. Zhou, R. K. W. Yu, C. S. Lee and S. T. Lee, *Thin Solid Films*, 2000, **368**, 222-226.
68. K.-T. Ho, S. Mi, M. Kiss, A. Toros and N. Quack, Lausanne, 2019.
69. A. Toros, M. Kiss, T. Graziosi, S. Mi, R. Berrazouane, M. Naamoun, J. Vukajlovic Plestina, P. Gallo and N. Quack, *Diamond and Related Materials*, 2020, **108**, 107839.
70. L. Olano, M. E. Dávila, J. R. Dennison, P. Martín-Iglesias and I. Montero, *Scientific Reports*, 2019, **9**, 13967.
71. O. Beyssac and M. Lazzeri, *European Mineralogical Union Notes in Mineralogy*, 2012, **12**, 415-454.
72. M. Bernard, A. Deneuville and P. Muret, *Diamond and Related Materials*, 2004, **13**, 282-286.
73. V. Mortet, A. Taylor, Z. Vlčková Živcová, D. Machon, O. Frank, P. Hubík, D. Tremouilles and L. Kavan, *Diamond and Related Materials*, 2018, **88**, 163-166.
74. P. W. May, W. J. Ludlow, M. Hannaway, J. A. Smith, K. N. Rosser and P. J. Heard, *MRS Online Proceedings Library*, 2008, **1039**, 1703.
75. R. Zulkharnay, W. Greenwood, A. Wood, J. Laverock and N. A. Fox, *ACS Applied Materials & Interfaces*, 2026, **18**, 9032-9042.
76. S. Ullah, L. Cullingford, T. Zhang, J. R. Wong, G. Wan, M. Cattelan and N. Fox, *MRS Advances*, 2021, **6**, 311-320.
77. J. Han, J.-Y. Lee, H. Kwon and J.-S. Yeo, *Nanotechnology*, 2014, **25**, 145604.
78. V. V. Dvorkin, N. N. Dzbanovsky, N. V. Suetin, E. A. Poltoratsky, G. S. Rychkov, E. A. Il'ichev and S. A. Gavrilov, *Diamond and Related Materials*, 2003, **12**, 2208-2218.
79. H. van der Graaf, H. Akhtar, N. Budko, H. W. Chan, C. W. Hagen, C. C. T. Hansson, G. Nützel, S. D. Pinto, V. Prodanović, B. Raftari, P. M. Sarro, J. Sinsheimer, J. Smedley, S. Tao, A. M. M. G. Theulings and K. Vuik, *Nuclear Instruments and Methods in Physics Research Section A: Accelerators, Spectrometers, Detectors and Associated Equipment*, 2017, **847**, 148-161.
80. J. Cazaux, *Nuclear Instruments and Methods in Physics Research Section B: Beam Interactions with Materials and Atoms*, 2006, **244**, 307-322.
81. J. Smedley, I. Ben-Zvi, J. Bohon, X. Chang, R. Grover, A. Isakovic, T. Rao and Q. Wu, *MRS Proceedings*, 2011, **1039**.
82. E. Wang, I. Ben-Zvi, A. Burrill, J. Kewisch, X. Chang, T. Rao, J. Smedley, Q. Wu, E. Muller and T. Xin, Report Number: BNL--94161-2011-CP, United States, 2011.